Synthesis and Evaluation of Cu/SAPO-34 Catalysts for NH$_3$-SCR

2: Solid-state Ion Exchange and One-pot Synthesis

Feng Gao*, Eric D. Walter, Nancy M. Washton, János Szanyi, and Charles H.F. Peden*

Institute for Integrated Catalysis, and Chemical & Materials Sciences Division, Pacific Northwest National Laboratory, P.O. Box 999, Richland, WA 99352, United States

* Corresponding authors. Email addresses: feng.gao@pnnl.gov (F. Gao); chuck.peden@pnnl.gov (C.H.F. Peden).

Abstract:

Cu/SAPO-34 catalysts are synthesized using two methods: solid-state ion exchange (SSIE) and one-pot synthesis. SSIE is conducted by calcining SAPO-34/CuO mixtures at elevated temperatures. For the one-pot synthesis method, Cu-containing chemicals (CuO and CuSO$_4$) are added during gel preparation. A high-temperature calcination step is also needed for this latter method. Catalysts are characterized with surface area/pore volume measurements, temperature programmed reduction (TPR), electron paramagnetic resonance (EPR) and nuclear magnetic resonance (NMR) spectroscopies, and scanning electron microscopy (SEM). Catalytic properties are examined using standard ammonia selective catalytic reduction (NH$_3$-SCR) and ammonia oxidation reactions. For Cu/SAPO-34 samples prepared by SSIE, Cu presents both as isolated Cu^{2+} ions and unreacted CuO. The former are highly active and selective in NH$_3$-SCR, while the latter catalyzes a side reaction; notably, the non-selective oxidation of NH$_3$ above 350 °C. Using the one-pot method followed by a high-temperature aging treatment, it is possible to form Cu/SAPO-34 samples with predominately isolated Cu^{2+} ions at low Cu loadings. However at much higher Cu loadings, isolated Cu^{2+} ions that bind weakly with the CHA framework and CuO clusters also form. These Cu moieties are very active in catalyzing non-selective NH$_3$ oxidation above 350 °C. At very low reaction temperature temperatures (< 155 °C), standard NH$_3$-SCR over Cu/SAPO-34 catalysts appears to be kinetically limited. However at higher temperatures, multiple rate limiting factors are possible.

Key words: Selective catalytic reduction, chabazite, SAPO-34, Cu/SAPO-34, diesel engine, emission control, NO$_x$

1. Introduction

Cu/SAPO-34 is one of the Cu/Chabazite catalysts that are currently commercialized as selective catalytic reduction (SCR) catalysts for diesel engine exhaust after-treatment. It has been known for some time, however, that Cu/SAPO-34 synthesis using a traditional aqueous solution ion exchange (IE) method is not straightforward [1-3]. This is due primarily to the fact that SAPO-34 undergoes facile irreversible hydrolysis during IE, leading to catalysts with low specific surface areas, micropore volumes and poor crystallinity. In our first paper of this series [4], Cu/SAPO-34 formation via aqueous solution IE was systematically studied using SAPO-34 samples synthesized with various structure-directing agents (SDAs). Interestingly, we found that the extent of irreversible hydrolysis depends strongly on two factors: Si-O-Al bond density within the SAPO framework, and zeolite framework stress. During solution IE, a SAPO-34 sample with higher Si-O-Al bond density and framework stress decomposes much more readily than a sample with low Si content and relatively low crystallinity. Regardless of the SAPO-34 substrate used, a high-temperature (e.g., 800 °C) aging treatment inevitably leads to substantial surface area and pore volume loss for Cu/SAPO-34 samples generated using this method [4]. It should be emphasized that Cu/SAPO-34 catalysts formed with solution IE are still highly active and selective in NH_3-SCR. *However, samples synthesized using this method cannot be considered very well-defined for fundamental and lab-to-lab comparative studies.*

To circumvent issues associated with solution IE, two alternative synthesis methods, one-pot synthesis and solid-state ion exchange (SSIE), are considered here. In one-pot synthesis, Cu-containing chemicals are introduced in the gel preparation step prior to hydrothermal synthesis. These could be Cu salts or CuO [5], or Cu-containing SDAs [6,7]. Following the synthesis and calcination steps, one obtains Cu/SAPO-34 directly. SSIE is a commonly used method to introduce charge compensating cations in zeolites [8]. Typically, zeolites and metal

halides are thoroughly mixed together and the mixture is heated to elevated temperatures in flowing inert gas or vacuum to facilitate ion exchange. Alternatively, SSIE can be performed by passing metal halide vapors through a zeolite bed held at a certain elevated temperature. When zeolites are in hydrogen or ammonium forms, SSIE is particularly suitable since the hydrogen halides generated are readily removed. This allows high exchange levels that are generally difficult for solution IE. To our knowledge, Cu/SAPO-34 formation via SSIE first appeared in the open literature in 1992 [9]. In the present study we systematically investigated SSIE and one-pot methods in Cu/SAPO-34 formation with the aims of: *(1)* providing simple yet efficient methods that can be readily reproduced by other researchers; and *(2)* generating model catalysts (e.g., samples with solely isolated Cu^{2+} ions) that are suitable for structure-function relationship type of studies. The model catalysts thus generated were further tested for NH_3-SCR to probe such relationships.

2. Experimental

2.1 Catalyst synthesis

As is well-known, SAPO-34 can be synthesized with various Si/Al/P precursors, gel compositions and SDAs. Minor structural differences in SAPO-34 samples, however, may have profound effects on their catalytic behavior [10,11]. Therefore, five different SAPO-34 substrates were used in the SSIE section. However, for the sake of simplicity, only two are discussed in detail below. One of these samples was purchased from ACS Material®, and is denoted here as SAPO-34-ACS. The other was prepared in-house, using morpholine (MOR) as SDA, 85% o-phosphoric acid as the P source, aluminum hydroxide as the Al source, and fumed silica as the Si source. Poly(ethylene glycol), PEG-400, was also used as a crystal growth inhibitor (CGI) to generate uniform and small particles [12]. All chemicals used in our syntheses were purchased

from Sigma-Aldrich with purities of analytical grade or better. This sample is denoted as SAPO-34-MOR. More details for the preparation this sample and other in-house synthesized SAPO-34 samples have been published elsewhere [4]. Table 1 lists the initial gel composition prior to synthesis of SAPO-34-MOR, and BET surface areas and micropore volumes (from the t-plot method) of the two SAPO-34 samples measured with a Quantachrome Autosorb-6 analyzer and using liquid nitrogen. Note that surface areas and pore volumes of these two samples are almost identical. This was one of the main reasons that these two substrates were chosen for detailed comparison. We also used three other in-house samples for SSIE and these are detailed in the Supplementary Information (SI-1). SEM images for all of the SAPO-34 samples are also shown in SI-1.

SSIE was first tested by thoroughly mixing anhydrous $CuCl_2$ and SAPO-34, and then the mixture was slowly heated in a tube furnace under dry N_2. Unfortunately, SAPO-34 completely decomposed in this process. Presumably, an acidic environment, formed by the dissolution of the generated HCl into residual H_2O, led to SAPO-34 decomposition. Our control experiments show that SAPO-34 readily decomposes in hot acid solutions. Next, nanosized CuO (Sigma-Aldrich, average particle size ~50 nm, confirmed from our own XRD analysis using the Scherrer equation) was used as the Cu source. In this case, SAPO-34 and CuO powders were thoroughly mixed inside a mortar and the mixtures were calcined in air at various elevated temperatures for various periods. Cu/SAPO-34 catalysts were successfully synthesized via this method.

During one-pot synthesis, $CuSO_4$ and CuO were chosen as the Cu sources. $CuSO_4$ could be added directly at any stage of the gel preparation. However, CuO must first be dissolved in phosphoric acid. More details regarding gel preparation can be found elsewhere [5]. After hydrothermal synthesis at 200 °C for 30 h under continuous stirring, the solids were separated from the mother liquid *via* centrifugation and washed with deionized water for 3 times. Finally,

they were dried at 120 °C under flowing N_2 and calcined in air at 600 °C for 5 h. A portion of the samples were further calcined in air at 800 °C for 16 h.

2.2 Catalyst characterization

Cu contents of the Cu/SAPO-34 samples were determined with Inductively Coupled Plasma Atomic Emission Spectroscopy (ICP-AES) conducted at Galbraith Laboratories (Knoxville, TN, USA). Prior to measurements, the samples were partially dehydrated at 150 °C for 2 h in vacuum to remove adsorbed moisture. BET surface areas and t-plot method micropore volumes of the samples were measured with a Quantachrome Autosorb-6 analyzer. Prior to analysis, the samples were dehydrated under vacuum overnight at 250 °C. Temperature-programmed reduction (TPR) was performed on a Micromeritics AutoChem II 2920 analyzer. After purging the hydrated samples (i.e., samples stored in air and, thus, saturated with moisture) with pure N_2 at 10 mL/min at room temperature for 30 min, TPR was carried out in 5% H_2/Ar at a flow rate of 30 mL/min. Temperature was ramped linearly from ambient to 800 °C at 10 °C/min and H_2 consumption was monitored with a TCD detector. 50mg of catalyst was used for each H_2-TPR experiment. Powder X-ray diffraction (XRD) measurements were performed on a Philips PW3040/00 X'Pert powder X-ray diffractometer with Cu K_α radiation (λ = 1.5406 Å). Data were collected with 2θ ranging from 5° to 50° with a step size of 0.02°. Scanning Electron Microscopy (SEM) was conducted on a FEI Helios 600 FIB-SEM instrument. Samples were mounted on a carbon tape and 5nm of carbon was deposited onto the samples for conductivity. Imaging was done at 5 keV. Electron paramagnetic resonance (EPR) and nuclear magnetic resonance (NMR) experimental details have been described elsewhere [4].

2.3 SCR and NH_3 oxidation reaction tests

NH_3-SCR reaction kinetics were measured using a plug-flow reaction system described elsewhere [4]. Powder samples were pressed, crushed and sieved (60-80 mesh) prior to use. For

standard SCR, the feed gas contained 350 ppm NO, 350 ppm NH_3, 14% O_2, 2.5% H_2O and balance N_2. NH_3 oxidation reactions were conducted in the same manner without NO_x. Stoichiometries for these reactions are shown below:

Standard SCR reaction: $4NH_3 + 4NO + O_2 = 4N_2 + 6H_2O$;

NH_3 oxidation reaction: $4NH_3 + 3O_2 = 2N_2 + 6H_2O$.
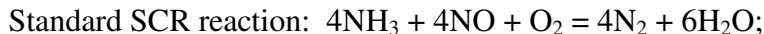
All of the gas lines were heated to over 100 °C to avoid water condensation. The total gas flow was 300 sccm, and the gas hourly space velocity (GHSV) was estimated to be ~400,000 h^{-1} for a catalyst amount of 30 mg. Concentrations of reactants and products were measured by an online Nicolet Magna 560 FTIR spectrometer with a 2 m gas cell maintained at 150 °C.

For temperature-dependent steady-state reaction measurements, the catalysts were first activated in 14% O_2/N_2 flow for 1 hr at 550 °C. Following which, NO, NH_3 and H_2O were added to the feed to start the SCR reaction. At each target temperature, a minimum waiting time of ~45 min was applied to insure steady-state reaction. NO_x and NH_3 conversions were calculated based on the following equations:

$$NO_x\ Conversion\ \% = \frac{(NO+NO_2)_{inlet}-(NO+NO_2+N_2O)_{outlet}}{(NO+NO_2)_{inlet}} \times 100$$

$$NH_3\ Conversion\ \% = \frac{(NH_3)_{inlet}-(NH_3)_{outlet}}{(NH_3)_{inlet}} \times 100$$

3. Results

3.1 Solid-State Ion Exchange (SSIE)

3.1.1 Temperature Effects

Solid-state reaction between SAPO-34 and CuO can proceed *via* the following reaction pathway:

H-SAPO-34 + CuO → Cu/SAPO-34 +H_2O (stoichiometry: $2H^+ + CuO \rightarrow Cu^{2+} + H_2O$)

6
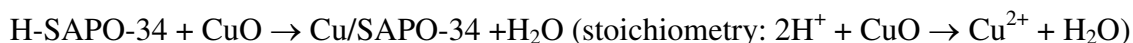
(Note that it is also possible for Cu to exchange with a single proton leading to $[Cu(OH)]^+$ or Cu^+ species at the zeolite ion exchange site. If the latter, Cu^+ could then react with H_2O at lower temperatures leading again to exchanged $[Cu(OH)]^+$.) Experiments were first carried out to determine temperatures needed for the reaction to proceed at appreciable rates. In this case, the SAPO-34-MOR sample was mixed with CuO (15 mg CuO per gram of SAPO-34, abbreviated as 15 mg/g) and the mixture was calcined at various temperatures and for different periods of time in air. Both TPR and EPR were used to monitor isolated Cu^{2+} ion formation. Figure 1(a) displays the TPR results. For the SAPO-34/CuO physical mixture, a single reduction state was found at ~258 °C. This was due unambiguously to $CuO \rightarrow Cu^0$. For the sample calcined at 600 °C for 5h, again a single reduction peak was found but the temperature shifted to ~270 °C. The TPR data for the sample calcined at 700 °C was very similar but a low-temperature shoulder feature started to develop, and for the samples calcined at 800 °C for various periods, reduction at ~240 °C became well-resolved. Based on previous studies, this reduction state was attributed to $Cu^{2+} \rightarrow Cu^+$ [13,14]. Therefore, the appearance of this reduction feature strongly indicates the formation of isolated Cu^{2+} via SSIE. In the meantime, the major reduction peak shifted gradually to higher temperatures (from ~287 to ~300 °C) as the calcination time increased perhaps due to changes in dispersion of the CuO nanoparticles. Figure 1(b) presents EPR spectra of the samples saturated with moisture in air (denoted as hydrated samples), with the results obtained at 120 K in order to limit the mobility of the Cu species. The spectrum of the physical mixture is not displayed since no EPR signal was observed. The amount of EPR active species (i.e., isolated Cu^{2+} ions) were quantified using standard solutions of Cu(II)-imidazole. These values are also tabulated in figure 1(b). Clearly, SSIE occurred as low as 600 °C, and more isolated Cu^{2+} ions were generated with higher temperatures and longer calcination times. Note that the total Cu loading in these samples was ~1.2 wt% (as confirmed from ICP; i.e., there was no Cu loss during SSIE). This

7

demonstrates that, even with the SSIE treatment at 800 °C for 16 h, only a portion of CuO (~67%) converted to isolated Cu^{2+} ions. The rest remained EPR silent, presumably as unreacted CuO particles as also evidenced by the continuing presence of the high (~300 °C) temperature TPR peak.

Because some of the SSIE conditions were rather harsh, XRD was used to monitor the integrity of the SAPO-34 structures after SSIE. As is well known, SAPO-34 is sensitive to water vapor at ambient conditions, and hydrolysis renders ~50% of crystallinity loss within one day, causing a dramatic reduction in XRD signal intensities. However, further signal intensity loss becomes undetectable for long periods [15]. For the purpose of direct comparison, all samples were stored under ambient conditions for more than 24 h prior to XRD experiments. We note also, however, that XRD signal intensities for SAPO-34 materials are also influenced by the use of different SDAs during synthesis. Therefore, one should be very careful in comparing XRD patterns to judge crystallinity for different SAPO-34 materials. As displayed in figure 2, the Chabazite XRD patterns maintained very well for all samples. It is worth noting that: *(1)* for the sample aged at 700 °C for 5 h and the samples aged at 800 ºC for 1 and 5 h, the crystallinity even somewhat increased. *(2)* For samples aged at 800 °C, a weak diffraction feature appeared at $2\theta = 21.3°$ that can be assigned to a tridimite (SiO_2) dense phase [16]. The formation of this phase indicates some SAPO-34 decomposition. However, the intensity of this feature did not increase with increasing calcination time, suggesting that only a small portion of highly defective SAPO-34 decomposed (as will be shown below, SEM measurements indicated that the smallest particles tended to decompose). *(3)* For all of the samples, extremely weak diffraction peaks were found at 35.4 and 38.0° attributable to CuO [17]. The detection of CuO was consistent with the incomplete reaction between SAPO-34 and CuO noted above. However, the extremely weak intensities and the possible overlap of SAPO-34 diffraction features at similar angles precluded

quantification of unreacted CuO using XRD. Finally, the BET and micropore surface areas and micropore volumes for the samples are listed in Table 2. It is seen from these values that the sample surface areas and pore volumes decreased monotonically as the calcination conditions became more severe. However, even for samples calcined at 800 °C, total surface areas were still dominated by micropore surface areas demonstrating the considerable thermal stability of the SAPO-34 structure. In other words, amorphous phase formation (which likely no longer possessed micropore structures) from SAPO-34 decomposition was insignificant. SCR activities for these samples will be described below.

3.1.2 Cu Loading Effects

Next, Cu loading effects were probed. In this case, SAPO-34-ACS was used as the substrate (SAPO-34-MOR led to similar results, data not shown) where 1 g of SAPO-34 was thoroughly mixed with various amounts of CuO and the mixtures were calcined at 800 °C for 16 h in air. From the XRD patterns shown in figure 3(a), the Chabazite structures maintained rather well in all cases. However, for the Cu/SAPO-34 sample prepared using the largest amount of CuO (bottom spectrum, denoted as the 60.0 mg/g sample), CuO diffraction peaks were clearly detected demonstrating that substantial amounts of CuO remained unreacted. Meanwhile, a rather strong tridimite diffraction feature was detected (marked with an asterisk) for this sample. This suggests that CuO, when present in excess amounts, promotes SAPO-34 decomposition. Figure 3(b) presents the corresponding TPR profiles. Clearly, the amount of isolated Cu^{2+} ions (represented by the reduction peak at ~250 °C for $Cu^{2+} \rightarrow Cu^+$) increased with increasing Cu loadings. However, even at the lowest Cu loading (5.75 mg/g), SSIE was incomplete as indicated by the TPR feature above 300 °C likely due to reduction from unreacted CuO to Cu^0. Moreover, for the 60.0 mg/g sample, a broad high-temperature reduction peak was also found (centered at ~500 °C). In line with the appearance of a tridimite (SiO_2) phase for this sample as shown in

9

figure 3(a), we tentatively assign this to reduction of a copper aluminate phase formed during the partial decomposition of SAPO-34. Table 3 lists the BET/micropore surface areas and micropore volumes for this series of samples. Consistent with the XRD and TPR data shown in figure 3, samples with lower Cu loadings displayed high (and similar) surface areas and pore volumes while the 60.0 mg/g sample has substantially smaller surface areas and pore volumes, due apparently to partial decomposition of SAPO-34.

Again, EPR was applied to quantify isolated Cu^{2+} ions generated in this series of samples. Hydrated samples were used to avoid the possible formation of EPR silent Cu^{+} ions during dehydration treatments. The spectra are displayed in figure 4(a). The amounts of EPR active isolated Cu^{2+} ions are also tabulated in this figure. Interestingly, for the 60.0 mg/g sample, a new high-field feature was found at ~3310 Gauss (marked with an asterisk). Note that this feature did not appear for lower Cu loading samples. An insert in figure 4(a), displaying the first-derivatives of the 30.4 and 60.0 mg/g spectra, more convincingly highlight the presence of this new feature. In line with the XRD and TPR data shown in figure 3, we tentatively assign this new feature to a Cu species in copper aluminate. Recently, Deka et al. [7] suggested that this copper aluminate species should be $CuAlO_2$, based on their EXAFS results. However, since our EPR results clearly show that Cu in this species is paramagnetic (i.e., Cu^{2+} instead of Cu^{+}), $CuAl_2O_4$ appears to be stoichiometrically more likely. However, $CuAl_2O_4$ can have Cu-Cu bonds where antiferromagnetic coupling may lead to loss of EPR signal. Very recently, Vennestrøm et al. [18] suggests that such species are most likely small clusters containing Cu and Al similar to $CuAl_2O_4$ without necessarily having Cu-Cu interactions. Therefore, this species is best described as "$CuAl_2O_4$-like". Figure 4(b) presents the relationship between total Cu loadings and EPR active Cu^{2+} ions in these samples (note that a new 45 mg/g sample was also used to provide an extra data point for this figure). The linear relationship suggests that SSIE rates between SAPO-34

10

and CuO are determined by the contact area between the two solids. This then indicates that better mixing between SAPO-34 and CuO, for instance with ball milling, or using SAPO-34 and CuO samples with smaller particle sizes, should facilitate SSIE. These issues, however, were not a primary focus for the present study.

Solid-state NMR was used to investigate the coordination of framework Al, P and Si for this series of samples, in order to gain more information on the Cu^{2+} ion-CHA framework interactions. Again, hydrated samples were used. Figure 5(a) presents the ^{27}Al spectra. Features at 43, 16 and -9 ppm are assigned to tetrahedrally, pentahedrally and octahedrally coordinated Al, respectively. We have shown previously that the formation of pentahedrally and octahedrally coordinated Al features is due to reversible SAPO-34 hydrolysis, and these features disappear upon dehydration [4]. From figure 5(a), all spectra are similar yet some subtle differences are noticeable: *(1)* the chemical shift for ^{27}Al in SAPO-34-ACS is found at 40 ppm while those for Cu-SAPO-34 are found at 43 ppm except for the 60mg/g sample, which also appeared at 40 ppm. Presumably, the slight chemical shift is caused by perturbations from extra framework Cu^{2+} ions in close proximity. It is rather curious that the 60mg/g sample did not follow this behavior. *(2)* A weak but clearly distinguishable feature is found at -57 ppm for the 60mg/g sample. For other samples, signal at this chemical shift is barely detectable. Most likely, this feature arises from Al-containing moieties due to SAPO-34 decomposition; e.g., $CuAl_2O_4$-like species. Figure 5(b) presents the ^{31}P spectra. Tetrahedrally coordinated P atoms are found at -28 ppm. A weak shoulder peak found at ~-20 ppm is assigned to framework P atoms perturbed with water. Upon dehydration, this shoulder peak disappears [4]. The corresponding ^{29}Si spectra are depicted in Figure 5(c). The main feature at -89 ppm is assigned to isolated tetrahedral Si atoms (i.e., $Si(OAl)_4$) while the -110 ppm peak is assigned to Si within silica islands (i.e., $Si(OSi)_4$) [15,19]. Note that, for the 60.0 mg/g sample, a marked intensity drop was found for the -89 ppm feature

while the intensity for the -110 ppm peak remained nearly constant. As was clear from figure 3(a), for this sample SAPO-34 partially decomposed to form a tridimite phase. The intensity drop for the -89 ppm feature is, therefore, likely due to formation of this phase. It has been shown previously that tridimite phases typically display ^{29}Si NMR signals from -110 to -116 ppm [20,21].

SSIE was also performed on our other in-house SAPO-34 samples and the resulting Cu/SAPO-34 catalysts were systemically characterized with surface area/pore volume measurements, XRD, H_2 TPR and EPR. For the sake of simplicity, these results are only shown in SI-2.

3.1.4 NH$_3$-SCR Kinetics

Figure 6(a) presents standard NH$_3$-SCR reaction kinetics on a Cu/SAPO-34-MOR catalyst (15mg/g, calcined at 800 °C for 5h, isolated Cu^{2+} ion content = 0.74 wt.%) at a moderate GHSV of 100,000 h^{-1}. From this graph, it can be seen that the light-off temperature occurs slightly below 200 °C, and NO$_x$ conversions and SCR selectivity were both essentially 100% for typical diesel engine operating temperatures (i.e., 200-300 °C). These results demonstrate that excellent Cu/SAPO-34 catalysts for NH$_3$-SCR can be generated using this, perhaps most straightforward Cu-SAPO-34 synthesis method. Only at 400 °C and above, due to occurrence of the non-selective NH$_3$ oxidation reaction, NO$_x$ conversions started to drop slightly. We note that under identical reaction conditions, Cu/SAPO-34 catalysts formed via traditional aqueous solution ion exchange show somewhat inferior performance [4]. However, at such a moderate GHSV, all of our SSIE samples (15mg/g) displayed essentially identical SCR performance as that shown for Cu/SAPO-34-MOR (15 mg/g) in figure 6(a).

To make more meaningful performance comparisons among samples, higher space velocities are required. In this case, it is necessary to first consider potential complexities caused

12

by mass transfer limitations. Using the 15mg/g Cu/SAPO-34-MOR sample, standard NH_3-SCR reactions were carried out at various space velocities and the results are displayed in figure 6(b). As expected, NO_x conversions increased as the space velocity decreased (i.e., NO_x residence time increased). Note that, at each reaction temperature and within the differential regime (NO_x conversions below ~15%, data points below the dashed horizontal line), NO_x conversions increased roughly by a factor of two as the residence times doubled. This demonstrates an absence of interparticle mass transfer limitations within the differential regime [22]. In the following, unless otherwise specified, SCR kinetics were measured at a GHSV of 400,000 h^{-1}, allowing us to rule out interparticle mass transfer limitations below a reaction temperature of ~160 °C where differential NO_x conversions are maintained.

Next, copper loading effects on SCR were probed using the Cu/SAPO-34-ACS series of samples. Figure 7 presents NO_x (a) and NH_3 (b) conversions during standard SCR as a function of reaction temperature for samples with various Cu loadings. For the 5.75 and 15.0 mg/g samples, NO_x and NH_3 conversion curves essentially completely overlap, indicating near 100% SCR selectivities at all reaction temperatures investigated. For samples with higher Cu loadings, this selectivity only held below ~350 °C. At higher temperatures, NH_3 conversions became significantly greater than NO_x conversions, and the difference became larger as the reaction temperature rose. As described above, these changes are due to the onset of non-selective NH_3 oxidation at high temperatures.

It has been proposed that isolated Cu^{2+} ions are the catalytically active centers for Cu/CHA catalysts in NH_3-SCR [23,24]. Assuming this to be the case, reaction rates can be normalized to turnover frequencies (TOF, mole NO_x per mole Cu^{2+} ion per second) using NO_x conversion data displayed in figure 7(a), and isolated Cu^{2+} ion loadings shown in figure 4(a). Figure 8 presents such TOFs as Arrhenius plots, where data only in the differential regime are

used. Interestingly, except for the partially decomposed 60.0 mg/g sample, all other samples displayed rather similar TOFs at each temperature and almost identical apparent reaction activation energies of E_a ~ 72 kJ/mol. It is also interesting to note that the 60.0 mg/g sample displayed TOFs roughly 50% lower at each temperature, but a higher apparent reaction activation energy of E_a ~ 89 kJ/mol. One possible explanation for the lower TOFs for the 60.0 mg/g sample is its partial zeolite structure decomposition.

NH_3-SCR kinetics were further investigated on 15 mg/g Cu/SAPO-34-ACS and Cu/SAPO-34-MOR samples at a GHSV of 400,000 h^{-1}. Note that detailed characterization results for these samples, as well as other 15mg/g SSIE samples studied here, are displayed in SI-2. Briefly, both samples maintained high crystallinity as judged from XRD, and their isolated Cu^{2+} ion loadings were 0.72 and 0.79 wt%, respectively, measured with EPR. Figure 9(a) depicts NO_x (lower panel) and NH_3 (upper panel) conversions during standard SCR as a function of temperature. Again, for each catalyst, NO_x and NH_3 conversion curves essentially overlapped below ~350 °C. Above 350 ºC, NH_3 conversions became slightly higher than NO_x conversions because of the extra NH_3 consumption via non-selective NH_3 oxidation. Interestingly, both samples gave almost identical NO_x (NH_3) conversions below ~155 °C while at higher temperatures, the activity for Cu/SAPO-34-MOR clearly surpassed Cu/SAPO-ACS. TOFs within the differential regime ($\leq$ 155 °C) were again calculated, and are displayed in figure 9(b) in the form of Arrhenius plots. As these two samples had almost identical isolated Cu^{2+} ion loadings, expectedly, TOFs at each temperature were very close, although the apparent reaction activation energy for Cu/SAPO-34-MOR (92 kJ/mol) is somewhat higher than Cu/SAPO-34-ACS (72 kJ/mol). We also studied SCR performance for our other two in-house Cu/SAPO-34 samples (also at 15mg/g). A more complete comparison among all 4 samples is detailed in SI-3.

To gain a better understanding of the performance differences between Cu/SAPO-34-ACS and Cu/SAPO-MOR, more characterizations were conducted. For example, to check for primary particle size effects, SEM imaging of the two catalysts was carried out and the results are shown in figure 10(a). Note first that the average particle size for Cu/SAPO-34-ACS was ~10 μm, twice the average Cu/SAPO-34-MOR particle size (~5 μm). For both samples, the majority of cubic SAPO-34 particles maintained rather well after the SSIE procedure (800 °C, 16 h), consistent with the XRD results. However in each sample, some very small particles indeed became irregular in shape indicating thermal damage. To elucidate the roles of catalyst acidity, NH_3 temperature-programmed desorption (TPD) was performed on the two Cu/SAPO-34 catalysts and the corresponding H/SAPO-34 substrates. As is shown in figure 10(b), NH_3 desorption states below ~300 °C are assigned to NH_3 desorption from Cu ions and other weaker (Lewis) acid sites, and peaks above ~350 °C due to NH_3 desorption from Brönsted acid sites. Estimated from their peak areas, Brönsted acid site density (i.e., framework charge density) for H/SAPO-34-ACS was approximately twice that for H/SAPO-34-MOR. For the SAPO-34-ACS samples, SSIE causes an expected decrease in desorption from Brönsted acid sites while enhancement in desorption from Cu/Lewis acid sites. However, this trend is not so clear for the SAPO-34-MOR samples. However, the results in figure 10(b) show that Cu/SAPO-34-ACS has substantially higher residual Brönsted acidity as compared to Cu/SAPO-34-MOR.

3.2 One-pot Synthesis

In this section, a one-pot Cu/SAPO-34 synthesis method and catalyst evaluations are addressed. There are two key questions for this method: *(1)* does the addition of Cu containing chemicals affect SAPO-34 formation during synthesis; and *(2)* what is the chemical and physical nature of Cu during and after synthesis? In the following synthesis example, Cu was introduced by dissolving CuO in phosphoric acid during gel preparation (gel composition: 1.0 SiO_2 : 0.83

15

P_2O_5 : 1 Al_2O_3 : 3 SDA : 60 H_2O : 0.006 CuO: 0.2 PEG-400; Morpholine was chosen as the SDA). The total Cu loading in the solid product was 0.32 wt.% from ICP-AES analysis. Figure 11(a) presents XRD patterns of the as-synthesized and calcined samples. Clearly, highly crystallizine SAPO-34 can still be synthesized in the presence of Cu. The product also shows excellent thermal stability at 800 °C where only a very small portion decomposes to give rise to the tridimite phase (marked with *). No CuO diffraction features were detected in these samples. Rather surprisingly, however, from the TPR spectra shown in figure11(b), the sample calcined at 600 °C (to burn off the SDA) gives an intense reduction peak at ~300 °C indicating that, in this sample, the majority of Cu is present as CuO rather than the targeted isolated Cu^{2+} ions. Following calcination at 800 °C for 16 h, the reduction curve broadens and the center shifts to ~250 °C indicating CuO conversion to isolated Cu^{2+} ions. Table 4 lists the surface areas and pore volumes of the two calcined samples at 600 and 800 °C, respectively.

The nature of the Cu species in the as-synthesized and calcined samples was further probed by EPR and the spectra are depicted in figure 12(a). Note first that the majority of Cu within the as-synthesized sample is in an EPR silent form (i.e., small CuO particles below XRD detection limits). Calcination at 600 °C and 800 °C resulted in Cu^{2+} formation, presumably via SSIE. The amounts of isolated Cu^{2+} ions in these samples were quantified using EPR and the results are also displayed in Table 4. By comparing the Cu contents determined using ICP-AES and EPR for the sample calcined at 800 °C, ~90% of Cu is present as isolated Cu^{2+} ions. Figure 12(b) presents standard NH_3-SCR reaction results for the sample calcined at 800 °C at a GHSV of 100,000 h^{-1}. Because of the low Cu loading, this sample did not show very good low-temperature performance as compared to the SSIE sample shown in figure 6(a). However, this sample shows excellent SCR selectivity as indicted by the almost identical NO_x and NH_3 conversions over the entire temperature range investigated. Above 400 °C, NO_x conversions

even become slightly higher than the corresponding NH_3 conversions. This may be due to NO_x overconsumption during Cu^{2+}/Cu^+ redox cycling [25].

As shown in figure 4(b), the rate of SSIE between SAPO-34 and CuO is determined by the contact area between the two solids. Using the commercial CuO nanoparticles (~50 nm), we were *unable* to achieve 100% conversion of CuO to isolated Cu^{2+} ions even at 800 °C for 16 h. On the other hand, better contact between CuO and SAPO-34 is expected in the one-pot synthesis method: from the one-pot synthesis example discussed above, although Cu mainly is present as CuO in the as-synthesized sample, CuO particle sizes must be substantially smaller than ~50 nm as they are undetectable with XRD. Indeed, for the one-pot sample described above, a calcination treatment at 800 °C for 16 h results in near complete CuO conversion to isolated Cu^{2+} ions. In the following, we attempt to use one-pot synthesis, followed by a high-temperature SSIE step, to generate Cu/SAPO-34 samples with predominately isolated Cu^{2+} ions, but with higher Cu loadings.

In this case, $CuSO_4$ was used as the Cu source during gel preparation according to the following composition: x $CuSO_4$: 1Al_2O_3: 0.85 P_2O_5: 0.6 SiO_2: 3 SDA: 60 H_2O. Five samples were prepared with x varying from 0.001 to 0.014. Figure 13(a) presents XRD patterns for the synthesized samples after calcining to 600 °C for 5 h to burn off the SDA (morpholine). All of the samples show high crystallinity. Adjacent to the XRD patterns of each sample, Cu loadings derived from ICP are also displayed. As expected, Cu loadings in the final products increase as more $CuSO_4$ is added to the gel. However, for the samples with the highest Cu loadings (1.89 and 3.16%), the appearance of CuO diffraction demonstrates formation of some rather large CuO particles. Figure 13(b) displays standard NH_3-SCR results at a GHSV of 100,000 h^{-1} for two of the samples with 0.90 and 3.15 wt.% Cu loadings. Apparently, the sample at higher Cu loading contains more isolated Cu^{2+} ions as it displays much better performance. However, this

performance was still inferior to a typical SSIE sample at the same GHSV (figure 6(a)) suggesting that, in both of these latter one-pot samples, isolated Cu^{2+} ion loadings were not high enough.

In order to convert more CuO to isolated Cu^{2+} ions, the sample with 3.15 wt.% Cu loading was further calcined in air at 800 °C for 16 h. The isolated Cu^{2+} ion loading in this thermally aged sample reaches 2.20 wt% as determined by EPR. Considering the fact that the amount of unreacted CuO (0.95 wt%) was still too high following this treatment, a hydrothermal aging treatment was applied next in order to convert even more CuO, based on the assumption that Cu^{2+} ion migration may be facilitated in the presence of moisture. Hydrothermal aging was performed by flowing zero air containing 10% (v/v) water vapor, through the sample placed in a quartz tube, also at 800 °C for 16 h. The isolated Cu^{2+} ion loading in this hydrothermally aged sample indeed became substantially higher (reached 2.65 wt%, ~84% of total Cu) as determined with EPR. Figure 14(a) presents the corresponding XRD patterns. Note from these XRD patterns that: *(1)* the crystallinity for the samples maintains reasonably well following both thermal and hydrothermal aging treatments; *(2)* aging treatments resulted in the disappearance of the CuO diffraction peaks; and *(3)* for the hydrothermally aged sample in particular, the intensity of the diffraction peak at ~9.5° (diffraction from the (100) plane of the CHA crystal) decreases dramatically. The origin for this latter result will be discussed in more detail below.

Figure 14(b) presents comparative standard NH_3-SCR reaction results at a GHSV of 400,000 h^{-1} for the fresh (calcined at 600 °C) and hydrothermally aged samples with 3.15 wt.% Cu loading. Despite the presence of more CuO in the fresh sample, SCR selectivity is excellent below 400 °C. However, for the hydrothermally aged sample (~84% of Cu present as isolated Cu^{2+} ions), the competing non-selective NH_3 oxidation reaction already becomes rather

significant at 350 °C, causing NO_x conversions to decrease. At higher temperatures, SCR selectivity becomes even worse.

4. Discussion

4.1. Comparison among Cu-SAPO-34 synthesis methods

In the first paper of this series, we focused on Cu/SAPO-34 synthesis via traditional aqueous solution ion exchange [4]. Highly active SCR catalysts can be generated using this method since Cu is mainly present as isolated Cu^{2+} ions, the active Cu moieties for NH_3-SCR. While others [13,14] have also had success preparing active Cu/SAPO-34 catalysts with aqueous ion exchange, the main drawback we found for this method, however, is that during solution ion exchange, the SAPO-34 framework always partially decomposes due to irreversible hydrolysis. A high-temperature aging treatment following solution ion exchange then inevitably leads to substantial surface area/pore volume loss. We show in this publication that this problem can be circumvented with SSIE and one-pot synthesis methods. Moreover, these methods also allow for straightforward Cu loading variations. In our SSIE method, figure 4(b) shows that the amount of isolated Cu^{2+} ions formed is proportional to the amount of CuO added to the SAPO-34/CuO mixture. Unfortunately, as the CuO particles we used in the present study were rather large (~50 nm), and because the SSIE process between SAPO-34 and CuO is quite slow, even reaction at 800 °C for 16 h was insufficient to convert all CuO particles. In principle, extending the reaction time may result in complete CuO conversion to isolated Cu^{2+} ions. However, at such a high temperature, SAPO-34 does degrade with time as evidenced from measurements of surface area and pore volume (Table 2). Still, our SSIE method is perhaps the most straightforward method to generate highly active catalysts for NH_3-SCR. Moreover, this method can be readily adapted by

19

other researchers for the preparation of "standard references" for comparative studies between samples generated using other methods. Using one-pot synthesis, the as-synthesized powders do not contain enough target isolated Cu^{2+} ions; as such, a high temperature treatment (i.e., an SSIE step) is needed to generate highly active catalysts (figure 12). In one-pot synthesis, although Cu mainly stays as CuO in the as-synthesized powders, their particle sizes can be substantially smaller than ~50 nm. In this case, the contact area between CuO and SAPO-34 is expected to increase, which benefits CuO conversion to isolated Cu^{2+} ions during the following SSIE step. Recently, Deka, et al. [7] also suggested that a more even distribution of Cu can be achieved from their one-pot synthesis method.

In the past a few years, several methods other than the traditional solution ion exchange have been tested by other researchers for Cu/SAPO-34 synthesis. Martínez-Franco, et al. studied one-pot synthesis using a Cu-containing SDA (Cu^{2+} with tetraethylenepentamine, Cu-TEPA) [6]. For the synthesis of Cu/SSZ-13, this method can be important since the much more expensive SDAs for SSZ-13 synthesis (e.g., *N*,*N*,*N*-trimethyl-1-adamantanamine iodide) can be avoided [26]. For SAPO-34 synthesis, where common and low cost SDAs (e.g., morpholine) are used, the advantage in this respect no longer exists. There is also a clear drawback when Cu-TEPA *alone* is used as the SDA: in the final product, the Cu content can too readily be excessive, because multiple SDA molecules are required to generate one CHA unit cell. In this study, we show clearly that excessive Cu loading is detrimental to the chemical and physical properties of Cu/SAPO-34 catalysts. In particular, high temperature (> 350 °C) SCR selectivity drops considerably at high Cu loadings (see, for example, figures 7(a) and 14(b)). Furthermore, SAPO-34 tends to partially decompose during high-temperature aging in the presence of excessive CuO (figure 3). Martínez-Franco, et al. also realized this problem and in their modified method, diethyl amine was used as a co-SDA to reduce Cu content in their final products. In one

synthesis example, these authors were able to generate Cu/SAPO-34 with a Cu loading of 3.4%, which maintained its structural integrity during hydrothermal aging at 750 °C. However, samples at higher Cu loadings decomposed under the same aging conditions [6]. In a very recent study by Wang, et al, CuC_2O_4 was introduced to SAPO-34 via a precipitation method [27]. Following a high-temperature aging treatment, active Cu/SAPO-34 catalysts can be generated. We note that this method follows the same mechanism as our more straightforward SSIE method; i.e., Cu-containing moieties reacting with SAPO-34 at elevated temperatures to form isolated Cu^{2+} ions. Deka, *et al* [7] also tried using chemical vapor deposition (CVD) with $Cu(NO_3)_2$ to generate Cu/SAPO-34. Unfortunately, SAPO-34 decomposed substantially during the process to a species identified by these authors as $CuAlO_2$ (although, judged from our EPR measurements, it is probably more $CuAl_2O_4$-like since Cu in this species is paramagnetic). Similarly, we were unable to form Cu/SAPO-34 using $CuCl_2$. In these latter two cases, the reason for failure is likely to be identical where the reaction products (HNO_3/HCl) dissolve in the moisture trapped inside the SAPO-34 cages creating an acidic environment that effectively promotes SAPO-34 hydrolysis.

We note that problems associated with the intrinsic moisture sensitivity of SAPO-34 [1-3] cannot be solved solely by avoiding the use of solution ion exchange to generate Cu/SAPO-34. In reality, Cu/SAPO-34 powders formed with one-pot methods or other "dry" methods will still have to be wash-coated to generate integrated $deNO_x$ catalysts. In application, these catalysts will still have to work in the presence of large amounts of moisture. Therefore, a better understanding and control of the moisture sensitivity of Cu.SAPO-34 catalysts will be as, if not more important than developing alternatives to solution ion exchange for Cu/SAPO-34 synthesis.

4.2. Roles of different Cu species and NH$_3$-SCR kinetics

There is considerable evidence that isolated Cu^{2+} ions are involved in Cu/CHA NH_3-SCR catalysts. Furthermore, both experimental studies from XRD [7,23] and X-ray absorption [24,28], and theoretical calculations [29] point to one generally agreed conclusion that Cu^{2+} ions prefer sites close to the face of double-6-membered rings (d6r) under fully dehydrated conditions. Here we wish to address a few more points: *(1)* upon saturation of sites next to d6r, Cu^{2+} ions can also occupy sites next to 8-membered rings [22,30]; *(2)* under humid NH_3-SCR reaction conditions, Cu^{2+} ions tend to move away from d6r, due to strong interactions between Cu^{2+} ions and NH_3/H_2O; and *(3)* even for Cu^{2+} ions next to d6r under dehydrated conditions, the situation is not simple because, depending on specific zeolite compositions, each 6-membered ring does not necessarily provide the same number of negative charges. To balance two negative framework charges, Cu(II) can exist as naked Cu^{2+} ions; however, if only one negative charge is needed to balance, Cu(II) is likely present as $[Cu(OH)]^+$ ions [31]. This difference is expected to greatly influence Cu^{2+} positioning and Cu^{2+}/Cu^+ redox processes. Besides isolated Cu ions, more recent spectroscopic studies seem to suggest that oxygen-bridged dicopper species (dimers) can also exist in Cu-CHA, especially at high Cu loadings and in the presence of oxygen [32,33]. In any case, it is important to realize that: *(1)* the nature of Cu^{2+} species changes as functions of Cu loading, framework charge, and the presence of various ligands; and *(2)* information derived using *ex situ* techniques from fully dehydrated samples may not be relevant for understanding the active Cu species under realistic NH_3-SCR reaction conditions.

Before more detailed discussions on roles of different Cu species, it is useful to first consider Cu loadings in commercial Cu/SSZ-13 and Cu/SAPO-34 catalysts. Note that the Cu loadings in the commercial catalysts are optimized, presumably from screening that give the best catalytic performance. From recent literature, Cu loading in a commercial Cu/SSZ-13 catalyst (nominal SiO_2/Al_2O_3 = 35) is ~2.8 wt%. This corresponds to ~100% ion exchange level (i.e.,

$\frac{mole\ fraction\ of\ Cu \times 2}{mole\ fraction\ of\ Al} \times 100\%$) [34]. In contrast, Cu loadings in commercial Cu/SAPO-34

catalysts are in the range of 1.5-2.0 wt% [35]. Using a rather conservative estimate of Si content

in SAPO-34 of ~5 wt% and assuming all Si atoms are isolated, ion exchange levels

($\frac{mole\ fraction\ of\ Cu \times 2}{mole\ fraction\ of\ Si} \times 100\%$) in commercial Cu/SAPO-34 catalysts are ~30%. The much

lower ion exchange levels for commercial Cu/SAPO-34 catalysts suggests the possibility that

higher Cu-loading Cu/SAPO-34 catalysts do not perform as well. Our kinetic data indicates that

this is indeed the case. Next we use our reaction kinetic data to discuss the various roles for

different Cu moieties in more detail.

It is worthwhile to first compare the characteristics of the standard NH_3-SCR reaction and

the major side reaction, non-selective NH_3 oxidation. Note that; *(1)* at lower temperatures,

standard NH_3-SCR is a much faster reaction than NH_3 oxidation; and (2) NH_3 oxidation is more

strongly activated than NH_3-SCR, therefore, its rate can become comparable to NH_3-SCR when

reaction temperatures are sufficiently high. Closer examination of the kinetic data displayed in

figures 7 and 14(b) reveals that, below ~300 °C, despite varying Cu loadings and synthesis

methods, all samples have excellent SCR selectivity as evidenced by the essentially identical

NO_x and NH_3 conversions. This means that, even for samples containing substantial amounts of

CuO (which is known to be a good NH_3 oxidation catalyst [36]), NH_3 oxidation rates are

negligible compared with NH_3-SCR at temperatures ≤ 300 °C.

Above 300 °C, the situation is much more complex. Qualitatively, the complexity derives

from the following: *(1)* unselective NH_3 oxidation is no longer negligible; and *(2)* different

Cu-containing moieties, namely, isolated Cu^{2+} ions at different locations of the CHA framework,

dicopper species, and CuO clusters with various sizes located both inside and outside CHA

cages, may exist simultaneously. All of these Cu moieties should be considered active for both

SCR and NH$_3$ oxidation reactions at such high temperatures; however, with very different (temperature dependent) selectivities [37-39]. With these in mind, we first consider the high-temperature catalytic properties of our most simple Cu/SAPO-34 model catalyst; i.e., the one-pot sample with a Cu loading of 0.32 wt% that had been aged at 800 °C for 16 h (figures 11, 12). In the fully hydrated form, the dominant Cu species within this sample are isolated Cu^{2+} ions (~90% of all Cu, judged from ICP-AES and EPR analyses), and the amount of EPR silent species is extremely small (~0.038 wt%). The TPR for this sample displayed in figure 11(b), also confirms isolated Cu^{2+} ions as the dominant Cu-species. In this regard, it is especially interesting to note from figure 12(b) that this sample maintains excellent SCR selectivity at temperatures much higher than 300 °C.

Next, the one-pot sample with the highest Cu loading (3.16 wt%, figures 13 and 14) is discussed. With the aid of hydrothermal aging, this sample also contains predominantly isolated Cu^{2+} ions (~84% of all Cu) and the amount of EPR silent species is reasonably low (0.63 wt%). Note that, prior to aging at 800 °C, this sample contains some large CuO particles, as evidenced from the XRD patterns shown in figure 13(a). Note also that diffraction from the (100) plane (the 9.6° feature) for the hydrothermally aged sample (figure 14(a)) decreased dramatically as compared with other diffraction peaks. This behavior strongly indicates that, after hydrothermal aging, a considerable amount of newly formed isolated Cu^{2+} ions are located inside the CHA cages next to 8-membered rings. This follows because these Cu^{2+} ions cause deformation of the 8-membered rings and, in turn, leads to a weakening of diffraction from the (100) plane of the Chabazite structure (SI-4). Overall, the high Cu-loading, hydrothermally aged sample contains two types of Cu moieties that other samples lack: *(1)* a considerable amount of isolated Cu^{2+} placed inside the CHA cages (i.e., next to 8-membered rings); and *(2)* a considerable amount of EPR silent species (presumably CuO clusters) sufficiently small so as to be below the detection

of XRD (although we cannot rule out the existence of dicopper species). Therefore, the poor SCR selectivities above ~300 °C for this sample shown in figure 14(b) are most certainly caused by non-selective NH_3 oxidation catalyzed by these EPR-silent Cu moieties. As mentioned earlier, commercial Cu/SAPO-34 catalysts contain rather low Cu loadings (< 2.0 wt%), considerably lower than commercial Cu/SSZ-13 catalysts in terms of ion exchange levels. One possible origin for this difference, as we suggested in the first paper of this series [4], is that SAPO-34 binds with isolated Cu^{2+} ions much weaker than SSZ-13. Indeed, isolated Cu^{2+} ions appear to be more readily reducible in SAPO-34 than in SSZ-13 as judged by TPR experiments [22,30]. Only at relatively low loadings, Cu^{2+} ions bind with the SAPO-34 framework strong enough to maintain good SCR selectivity (figure 12(b)). At higher Cu loadings, as discussed above, weakly bound Cu^{2+} ions and CuO clusters catalyze non-selective NH_3 oxidation efficiently above 300 °C. In contrast, isolated Cu^{2+} ions in Cu/SSZ-13 maintain high SCR selectivity at much higher ion exchange levels. The key origin for this difference is likely the average charge density difference between SSZ-13 and SAPO-34, as already suggested many years ago [40]. Overall, for optimal catalytic performance, Cu content in Cu/SAPO-34 should be high enough in order to have a sufficient number of catalytically active sites, yet low enough to avoid species that are highly active for side reactions (e.g., NH_3 oxidation).

Since NH_3 SCR reactions are highly exothermic [38], low NO_x conversions at relatively low reaction temperatures (e.g., < 160 °C) can only be explained by kinetic or mass-transfer limitations. In our recent study on Cu/SSZ-13 catalysts, we discovered that at low reaction temperatures (e.g., 150 °C) and above a certain ion exchange level (~23%), NO_x conversions did not continue to increase with increasing Cu loading [22]. There could be two explanations: *(1)* the newly added Cu^{2+} ions at higher loadings (presumably Cu ions located inside the CHA cages upon saturation of sites next to 6-membered rings [22,30]) are much less catalytically active; or

(2) SCR reaction becomes more severely limited by internal mass-transfer at high Cu loadings such that, as Cu loading rises, the efficiency of each Cu^{2+} ion decreases. In our prior studies, we preferred internal mass-transfer limitation as an explanation of such reaction behavior because we could not find any convincing evidence to suggest Cu^{2+} ions inside the CHA cages are less active than Cu^{2+} ions next to 6-membered rings [22,41].

In the present study of Cu/SAPO-34 catalysts, as displayed in figure 8, low-temperature SCR reaction over Cu/SAPO-34 appears to be kinetically limited as evidenced by the invariant TOFs at different isolated Cu^{2+} ion loadings. (Although the 60mg/g sample appears to be an exception, its lower activity is likely due to partial damage of the CHA structure.) It is also clear from figure 9(b) that kinetic limitations maintain at low reaction temperatures (< 155 °C) for samples synthesized using various SAPO-34 substrates. Because the rate limiting step(s) at such low reaction temperatures is (are) not clear at present, we are not in a position to rationalize the differences in low-temperature kinetics between Cu/SSZ-13 and Cu/SAPO-34 catalysts at this time.

Finally, it is worth comparing the SCR reaction results at high space velocities (shown in figure 9(a)) for the two catalysts prepared by SSIE, Cu/SAPO-34-ACS and Cu/SAPO-34-MOR. From EPR analyses, the two samples have almost identical isolated Cu^{2+} contents and, below ~155 °C, these two samples gave almost identical NO_x conversions. However, NO_x conversions on Cu/SAPO-34-MOR are substantially greater at higher reaction temperatures. One possible conclusion from this is that the rate limiting steps below and above ~155 °C are different. For example, a plausible rate limiting step that causes kinetic limitations below 155 °C is H_2O ligand desorption from Cu^{2+} ion sites, because NO_x and NH_3 may not have ready access to Cu^{2+} ion centers when they are fully surrounded by H_2O ligands. In this case, SCR reaction would only occur upon some H_2O ligand removal to leave open space for NO_x and NH_3 to adsorb and react.

Above ~155 °C, where Cu^{2+} ion centers are less inhibited by water and, meanwhile, water trapped within the CHA cages and channels becomes more mobile, other rate limiting factors can become dominant. On this basis, we suggest that the better performance for Cu/SAPO-34-MOR above 155 °C may be understood from the following considerations. *(1)* As displayed in figure 10(a), the average particle size for Cu/SAPO-34-ACS (~10 μm) is nearly twice that of Cu/SAPO-34-MOR (~5 μm). This may result in more efficient internal mass transfer for Cu/SAPO-34-MOR. Previous studies have shown that, for the methanol-to-olefin (MTO) reaction, SAPO-34 particle sizes must be reduced below 0.5μm in order to completely remove pore (i.e., *intra-crystalline*) diffusion limitations [42]. Although we do not have strong evidence to suggest that the NH_3-SCR reaction above 155 °C is solely limited by pore diffusion, we certainly cannot rule out its contribution. *(2)* As noted above, figure 10(b) shows that Cu/SAPO-34-ACS has substantially higher Brönsted acidity (as determined from the NH_3 desorption peak area) compared to Cu/SAPO-34-MOR. As such, our reaction data shown in figure 9(a) are not consistent with the "stronger Brönsted acidity, better SCR performance" behavior found by others [43]. Instead, besides the possible internal diffusion influences discussed above, another possible explanation is the difference in redox properties of the Cu ions.

As shown in figure 10(b), Brönsted acid site density for H/SAPO-34-ACS is roughly twice that for H/SAPO-34-MOR. In other words, framework charge density for SAPO-34-ACS is about two times that of SAPO-34-MOR. Framework charge density may have important influences on the catalytic performance of Cu/SAPO-34 samples. In a qualitative way, at similar Cu^{2+} ion loadings, a lower framework charge density would mean generally weaker electrostatic interactions between Cu^{2+} and the CHA framework. This, in turn, allows more facile Cu^{2+}/Cu^{+} redox cycling. Meanwhile, more weakly bound Cu^{2+} may migrate more readily and interact with each other to generate highly active dicopper species. Considering the above, the overall SCR

performance is clearly governed by multiple factors, and those that are rate determining can be very different under different reaction conditions. It is also apparent that much work is still needed to fully understand the true nature of the catalytically relevant Cu species for CHA-based SCR, as well as the various rate limiting factors under various reaction conditions. Prior to that, the development of structure-function relationships for Cu/SAPO-34 SCR systems remains difficult. Indeed, a primary purpose of the present study was to highlight the complexities of developing such a fundamental understanding due to difficulty of reproducibly preparing useful model Cu/SAPO-34 catalysts.

5. Conclusions

(1) Two alternative Cu/SAPO-34 synthesis methods, notably, solid-state ion exchange and one-pot synthesis, are used in the present study. Compared with the traditional solution ion exchange method, both SSIE and one-pot methods yield Cu/SAPO-34 samples with higher surface area/pore volumes and higher crystallinity.

(2) The roles for different Cu-containing moieties are discussed based on detailed reaction kinetics. Below ~300 °C, excellent NH_3-SCR selectivity maintains for all samples investigated. Above ~300 °C, CuO species and isolated Cu^{2+} ions that bind weakly with the SAPO-34 framework catalyze non-selective NH_3 oxidation leading to lower SCR selectivities. In contrast, isolated Cu^{2+} ions that bind strong with the CHA framework maintain excellent SCR selectivity.

(3) At very low reaction temperatures (< 155 °C), NH_3-SCR over our Cu/SAPO-34 samples appears to be kinetically limited, and H_2O ligand desorption from the catalytic centers may be the rate limiting factor. At higher reaction temperatures, SCR performance may be affected by multiple factors including internal (*intra-crystalline*) mass-transfer limitations, location and mobility of Cu ions, redox of Cu ions, and framework charge density of the CHA structure.

Acknowledgements

References

[1] Frache A, Palella BI, Cadoni M, Pirone R, Pastore HO, Marchese L (2003) Top Catal 22: 53-57.

[2] Akolekar DB, Bhargava SK, Foger K (1998) J Chem Soc Faraday Trans 94: 155-160.

[3] Akolekar DB, Bhargava SK (2001) Appl Catal A 207: 355-365.

[4] Gao F, Walker ED, Washton NM, Szanyi J, Peden CHF (2013) ACS Catal 3: 2083-2093.

[5] Bull I, Muller U (2011) European Patent 2269733.

[6] Martínez-Franco R, Moliner M, Franch C, Kustov A, Corma A (2012) Appl Catal B 127: 273-280.

[7] Deka U, Lezcano-Gonzalez I, Warrender SJ, Picone AL, Wright PA, Weckhuysen BM, Beale AM (2013) Microporous Mesoporous Mater 166: 144-152.

[8] Karge HG (2008) *Solid-State Ion Exchange in Zeolites*, in: Handbook of Heterogeneous Catalysis, Eds. Ertl G, Knözinger H, Schüth F, Weitkamp J 2nd Edition, WILEY-VCH, p484-510.

[9] Zamadics M, Chen XH, Kevan L (1992) J Phys Chem 96: 5488-5491.

[10] Wilson S, Barger P (1999) Microporous Mesoporous Mater 29: 117-126.

[11] Alvaro-Munoz T, Marquez-Alvarez C, Sastre E (2012) Catal Today 179: 27-34.

[12] Venna SR, Carreon MA (2008) J Phys Chem B 112: 16261-16265.

[13] Wang L, Li W, Qi GS, Weng D (2012) J Catal 289: 21-29.

[14] Xue JJ, Wang XQ, Qi GS, Wang J, Shen MQ, Li W (2013) J Catal 297: 56-64.

[15] Briend M, Vomscheid R, Peltre MJ, Man PP, Barthomeuf D (1995) J Phys Chem 99: 8270-8276.

[16] Frache A, Palella B, Cadoni M, Pirone R, Ciambelli P, Pastore HO, Marchese L (2002) Catal Today 75: 359-365.

[17] Kwak JH, Tran D, Burton SD, Szanyi J, Lee JH, Peden CHF (2012) J Catal 287: 203-209.

[18] Vennestrom PNR, Janssens TVW, Kustov A, Grill M, Puig-Molina A, Lundegaard LF, Tiruvalam RR, Concepcion P, Corma A (2014) J Catal 309:477–490.

[19] Tan J, Liu ZM, Bao XH, Liu XC, Han XW, He CQ, Zhai RS (2002) Microporous Mesoporous Mater 53: 97-108.

[20] Kitchin SJ, Kohn SC, Dupree R, Henderson CMB, Kihara K (1996) American Mineralogist 81: 550-560.

[21] Xiao Y, Kirkpatrick RJ, Kim YJ (1996) *American Mineralogist 78*: 241-244.

[22] Gao F, Walker ED, Karp EM, Luo JY, Tonkyn RG, Kwak JH, Szanyi J, Peden CHF (2013) J Catal 300: 20-29.

[23] Fickel DW, Lobo RF (2010) J Phys Chem C 114: 1633-1640.

[24] Deka U, Juhin A, Eilertsen EA, Emerich H, Green MA, Korhonen ST, Weckhuysen BM, Beale AM (2012) J Phys Chem C 116: 4809-4818.

[25] Kieger S, Delahay G, Coq B, Neveu B (1999) J Catal 183: 267-280.

[26] Ren LM, Zhu LF, Yang CG, Chen YM, Sun Q, Zhang HY, Li CJ, Nawaz F, Meng XJ, Xiao FS (2011) Chem Commun 47: 9789-9791.

[27] Wang L, Gaudet JR, Li W, Weng D (2013) J Catal 306: 68-77.

[28] Korhonen ST, Fickel DW, Lobo RF, Weckhuysen BM, Beale AM (2011) Chem Comm 47: 800-802.

[29] McEwen JS, Anggara T, Schneider WF, Kispersky VF, Miller JT, Delgass WN, Riberio FH (2012) Catal Today 184: 129-144.

[30] Kwak JH, Zhu HY, Lee JH, Peden CHF, Szanyi J (2012) Chem Comm 48: 4758-4760.

[31] Da Costa P, Moden B, Meitzner GD, Lee DK, Iglesia E (2002) Phys Chem Chem Phys 4: 4590-4601.

[32] Giordanino F, Vennestrøm PNR, Lundegaard LF, Stappen FN, Mossin S, Beato P, Bordiga S, Lamberti C (2013) Dalton Trans. 42: 12741-12761.

[33] Guo Q, Fan FT, Michel Ligthart DAJ, Li GN, Feng ZC, Hensen EJM, Li C (2014) Chem Cat Chem 6: 634-639.

[34] Schmieg SJ, Oh SH, Kim CH, Brown DB, Lee JH, Peden CHF, Kim DH (2012) Catal Today 184: 252-261.

[35] Kispersky VF, Kropf AJ, Ribeiro FH, Miller JT (2012) Phys Chem Chem Phys 14: 2229-2238.

[36] Kwak JH, Tonkyn R, Tran D, Mei DH, Cho SJ, Kovarik L, Lee JH, Peden CHF, Szanyi J (2012) ACS Catal 2: 1432-1440.

[37] Centi G, Perathoner S (1995) Appl Catal A 132: 179-259.

[38] Brandenberger S, Krocher O, Tissler A, Althoff R (2008) Catal Rev 50: 492-531.

[39] Deka U, Lezcano-Gonzalez I, Weckhuysen BM, Beale AM (2013) ACS Catal 3: 413-427.

[40] Zamadics M, Kevan L (1992) J Phys Chem 96: 8989-8993.

[41] Gao F, Kwak JH, Szanyi J, Peden CHF (2013) Top Catal 56: 1441-1459.

[42] Chen D, Moljord K, Fuglerud T, Holmen A (1999) Microporous Mesoporous Mater 29: 191-203.

[43] Wang J, Yu T, Wang XQ, Qi GS, Xue JJ, Shen MQ, Li W (2012) Appl Catal B 127: 137-147.

Tables

Table 1: Gel composition prior to synthesis for SAPO-34-MOR, and BET surface areas and pore volumes for SAPO-34-ACS and SAPO-34-MOR.

Sample	Gel composition	BET Surface Area (m^2/g)	Micropore Volume (cm^3/g)
SAPO-34-ACS	-	564	0.273
SAPO-34-MOR	$1Al_2O_3$: 0.85 P_2O_5: 1.0 SiO_2: 3 MOR: 0.2 PEG-400: 60 H_2O	549	0.268

Table 2: BET and micropore surface areas, and pore volumes for the Cu/SAPO-34-MOR samples calcined at varying conditions.

Sample	5-point BET surface area (m^2/g)	Micropore surface area (m^2/g)	Micropore volume (cm^3/g)
Mixture, RT	537	515	0.260
600 ºC, 5 h	564	538	0.272
800 ºC, 5 h	504	476	0.237
800 ºC, 1 h	472	447	0.225
800 ºC, 5 h	452	435	0.218
800 ºC, 16 h	391	370	0.187

Table 3: BET/micropore surface areas, pore volumes and EPR active Cu^{2+} ion loadings for the Cu/SAPO-34-ACS samples with various Cu loadings. All samples were calcined at 800 ºC for 16 h in air.

Sample (mg CuO/g)	5-point BET surface area (m^2/g)	Micropore surface area (m^2/g)	Micropore volume (cm^3/g)	EPR active Cu^{2+} ion (wt%)
5.75 mg/g	494	491	0.249	0.30
15.0 mg/g	443	442	0.235	0.72
30.4 mg/g	453	448	0.225	1.38
60.0 mg/g	309	306	0.156	2.31

Table 4: BET/micropore surface areas, pore volumes and EPR active Cu^{2+} ion loadings for the Cu/SAPO-34 samples formed via a one-pot method.

Sample	5-point BET surface area (m^2/g)	Micropore surface area (m^2/g)	Micro pore volume (cm^3/g)	EPR active Cu^{2+} ion (wt%)
One-pot, 600 ºC, 5 h	418	399	0.199	0.12
One-pot, 800 ºC, 16 h	380	350	0.174	0.29

Figure Captions

Figure 1

(a) Temperature-programmed reduction (TPR) data for the physical mixture of 15 mg CuO and 1g SAPO-34-MOR, and the Cu/SAPO-34 samples formed by calcining the mixture to various temperatures and time periods.

(b) The corresponding Electron Paramagnetic Resonance (EPR) spectra of the Cu/SAPO-34 samples formed by calcining the 15mg CuO + 1g SAPO-34-MOR mixture to various temperatures and time periods. The amounts of EPR active Cu^{2+} ions are also tabulated.

Figure 2

XRD patterns of the SAPO-34/CuO physical mixture and the SSIE samples. Calcination conditions are listed adjacent to the XRD patterns.

Figure 3

(a) XRD patterns of the Cu/SAPO-34 samples formed via SSIE using SAPO-34-ACS and various amounts of CuO. SSIE was conducted at 800 °C for 16 h in air. The samples are denoted as xx mg/g, denoting xx mg of CuO was mixed with 1 g of SAPO-34 prior to SSIE.

(b) The corresponding temperature-programmed reduction (TPR) curves for the samples shown in figure 3(a).

Figure 4

(a) Electron Paramagnetic Resonance (EPR) spectra of the Cu/SAPO-34 samples shown in figure 3. Samples were in the hydrated form prior to EPR measurements. The amounts of EPR active Cu^{2+} ions are also tabulated in this figure. Note that the 60.0 mg/g sample has an extra high-field feature at ~3310 G. Shown as an insert are the first-derivatives spectra for the 30.4 and 60.0 mg/g samples.

(b) EPR active Cu versus total Cu loadings for the Cu/SAPO-34 samples shown in figure3. Note that a new 45 mg/g samples was also used to obtain an extra data point for this figure.

Figure 5

(a) ^{27}Al, (b) ^{31}P and (c) ^{29}Si NMR spectra for the SAPO-34-ACS substrate and the SSIE samples. Hydrated samples were used for these measurements. Sample denotations are placed adjacent to the spectra.

Figure 6

(a) NO$_x$ (■) and NH$_3$ (●) conversion as a function of temperature on a Cu/SAPO-34-MOR sample formed by calcining a 15mg CuO/ 1g SAPO-34 mixture at 800 ºC for 5 h. Standard SCR reactant feed contains 350 ppm NO, 350 ppm NH$_3$, 14% O$_2$, 2.5% H$_2$O balanced with N$_2$. GHSV = 100,000 h^{-1}.

(b) NO$_x$ conversion as a function of temperature on a Cu/SAPO-34-MOR sample formed by calcining a 15mg CuO/1g SAPO-34 mixture at 800 ºC for 5 h. Standard SCR reactant feed contains 350 ppm NO, 350 ppm NH$_3$, 14% O$_2$, 2.5% H$_2$O balanced with N$_2$. Four different GHSVs are used at 800,000 (■), 400,000 (●), 200,000 (▲) and 100,000 (▼) h^{-1}, respectively.

Figure 7

(a) NO$_x$ and (b) NH$_3$ conversion as a function of temperature on Cu/SAPO-34-ACS samples formed by calcining xx mg CuO/1g SAPO-34 mixture at 800 ºC for 16 h. Standard SCR reactant feed contains 350 ppm NO, 350 ppm NH$_3$, 14% O$_2$, 2.5% H$_2$O balanced with N$_2$. Samples are denoted as 5.75 (■), 15.0 (●), 30.4 (▲) and 60.0 (♦) mg CuO/g, respectively. GHSV = 400,000 h^{-1}.

Figure 8

Arrhenius plots in the differential kinetic regime (< 160 C, NO$_x$ conversion ≤ 15%) using data displayed in figure 7(a). Note that reaction rates are converted to turnover frequencies (TOF, mole NO$_x$/mole Cu^{2+}/s). Samples are denoted as 5.75 (■), 15.0 (●), 30.4 (▲) and 60.0 (♦) mg/g, respectively.

Figure 9

(a) NO$_x$ and NH$_3$ conversion as a function of temperature on Cu/SAPO-34-ACS (■) and Cu/SAPO-34-MOR (●) samples formed by calcining 15 mg CuO/1g SAPO-34 mixtures at 800 ºC for 16 h. Standard SCR reactant feed contains 350 ppm NO, 350 ppm NH$_3$, 14% O$_2$, 2.5% H$_2$O balanced with N$_2$. GHSV = 400,000 h^{-1}.

(b) Arrhenius plots in the differential kinetic regime (< 160 °C, NO$_x$ conversion ≤ 15%) using data displayed in figure 9(a). Note that reaction rates are converted to turnover frequencies (TOF, mole NO$_x$/mole Cu^{2+}/s).

Figure 10

(a) SEM images of Cu/SAPO-34-ACS and Cu/SAPO-34-MOR samples formed by calcining 15 mg CuO/1g SAPO-34 mixtures at 800 °C for 16 h. Scale bars are 50 μm.

(b) NH_3 TPD of H/, Cu/SAPO-34-ACS and H/, Cu/SAPO-34-MOR. NH_3 was adsorbed at 100 °C until saturation. After purging with dry N_2 at the same temperature for 1 h to remove weakly adsorbed species, temperature was ramped to ~800 °C at 10 °C/min.

Figure 11

(a) XRD patterns for the one-pot samples formed using CuO as a Cu source during gel preparation. The as-synthesized sample (dried, prior to SDA removal) and the calcined samples at 600 °C for 5 h, and 800 °C for 16 h are displayed.

(b) TPR curves for the calcined samples.

Figure 12

(a) EPR spectra for the one-pot samples formed using CuO as a Cu source during gel preparation. The as-synthesized sample (dried, prior to SDA removal) and the calcined samples at 600 °C for 5 h, and 800 °C for 16 h are displayed.

(b) NO_x (■) and NH_3 (●) conversion as a function of temperature on the one-pot sample formed using CuO as the Cu source and calcined at 800 °C for 16 h after synthesis. Standard SCR reactant feed contains 350 ppm NO, 350 ppm NH_3, 14% O_2, 2.5% H_2O balanced with N_2. GHSV = 100,000 h^{-1}.

Figure 13

(a) XRD patterns for the one-pot samples formed using various amounts of $CuSO_4$ as the Cu source during gel preparation. All samples are calcined at 600 °C for 5 h prior to XRD measurements. Cu loadings, derived from ICP-AES analysis, are displayed adjacent to the corresponding patterns.

(b) NO_x conversion as a function of temperature on two of the one-pot samples formed using $CuSO_4$ as the Cu source and calcined at 600 °C for 5 h after synthesis. The total Cu loadings in these samples are 0.90 (■) and 3.15 (●) wt.%, respectively. Standard SCR reactant feed contains 350 ppm NO, 350 ppm NH_3, 14% O_2, 2.5% H_2O balanced with N_2. GHSV = 100,000 h^{-1}.

Figure 14

(a) XRD patterns for the one-pot sample containing 3.15 wt.% Cu formed using $CuSO_4$ as the Cu source during gel preparation. The fresh sample (calcined at 600 °C for 5 h) and two aged samples, one thermally at 800 °C for 16 h in air and one hydrothermally aged at 800 °C for 16 h in the presence of 10% H_2O vapor, are displayed.

(b) NO_x (■) and NH_3 (●) conversion as a function of temperature on the one-pot sample 3.15 wt.% Cu formed using $CuSO_4$ as the Cu source during gel preparation. The upper panel shows the hydrothermally aged sample and the bottom panel shows the fresh sample. Standard SCR reactant feed contains 350 ppm NO, 350 ppm NH_3, 14% O_2, 2.5% H_2O balanced with N_2. GHSV = 400,000 h^{-1}.

(a)
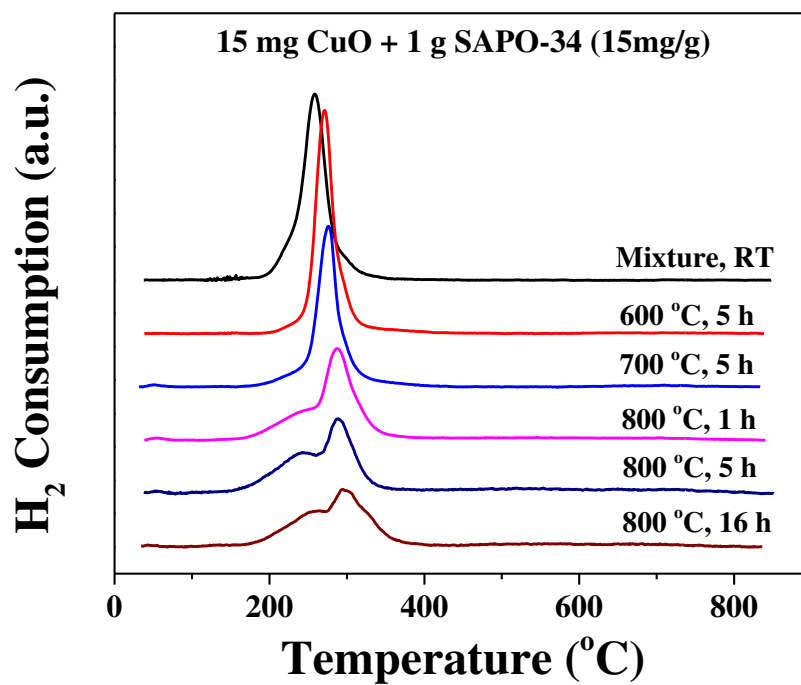
(b)
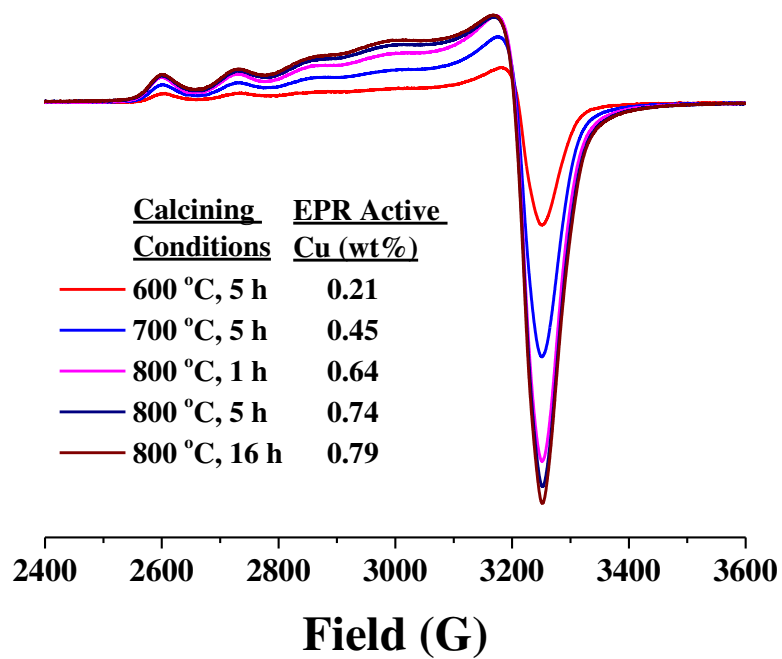
Figure 1, Gao, Walter, Washton, Szanyi, Peden
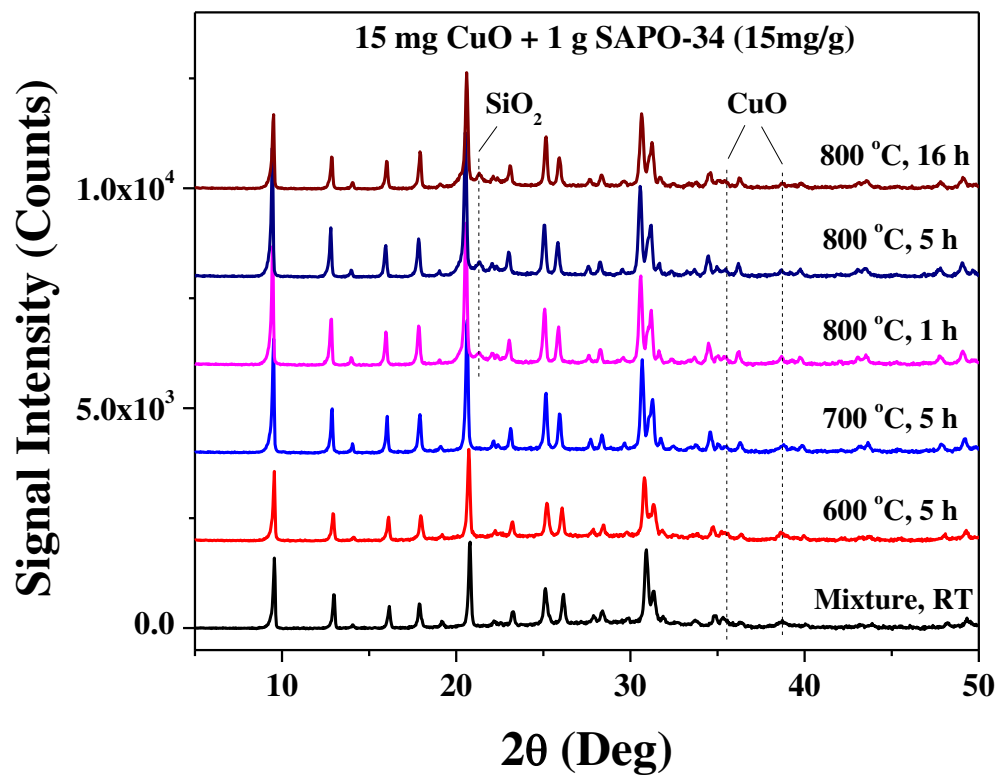
Figure 2, Gao, Walter, Washton, Szanyi, Peden

(a)
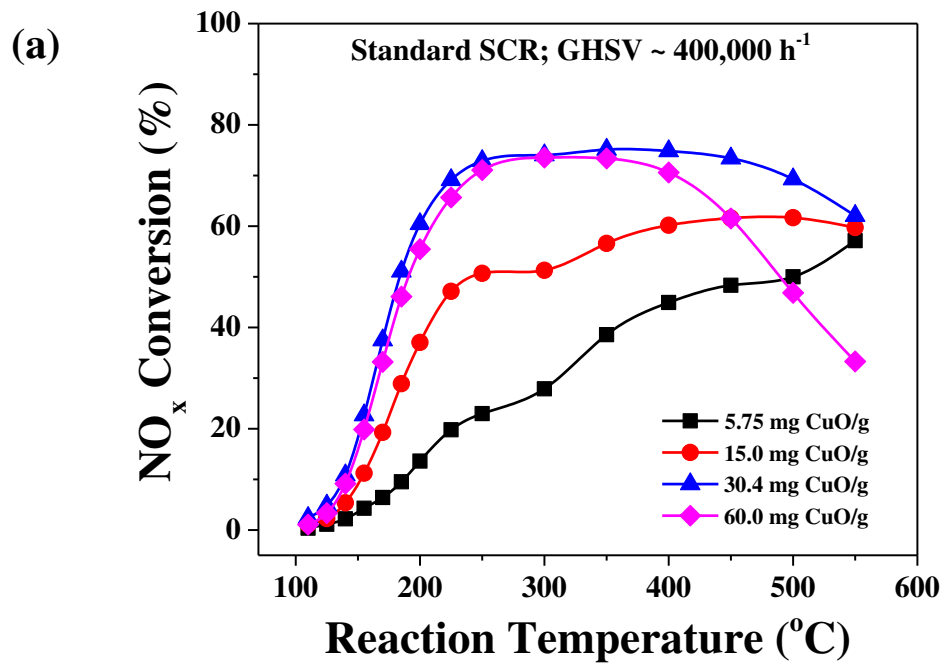
(b)
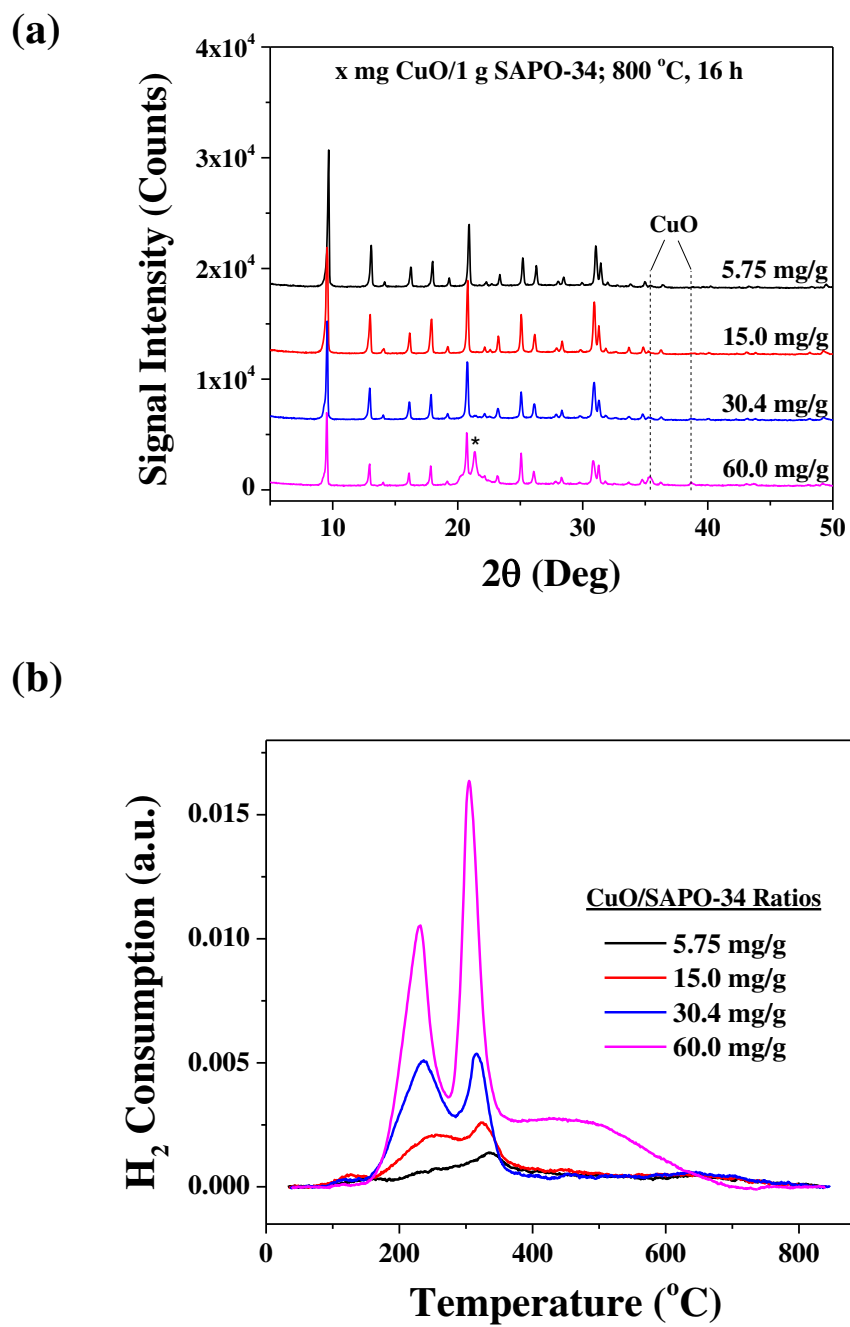
Figure 3, Gao, Walter, Washton, Szanyi, Peden

(a)

CuO/SAPO-34 Ratios	EPR Active Cu (wt%)
5.75 mg/g	0.30
15.0 mg/g	0.72
30.4 mg/g	1.38
60.0 mg/g	2.31

(b)
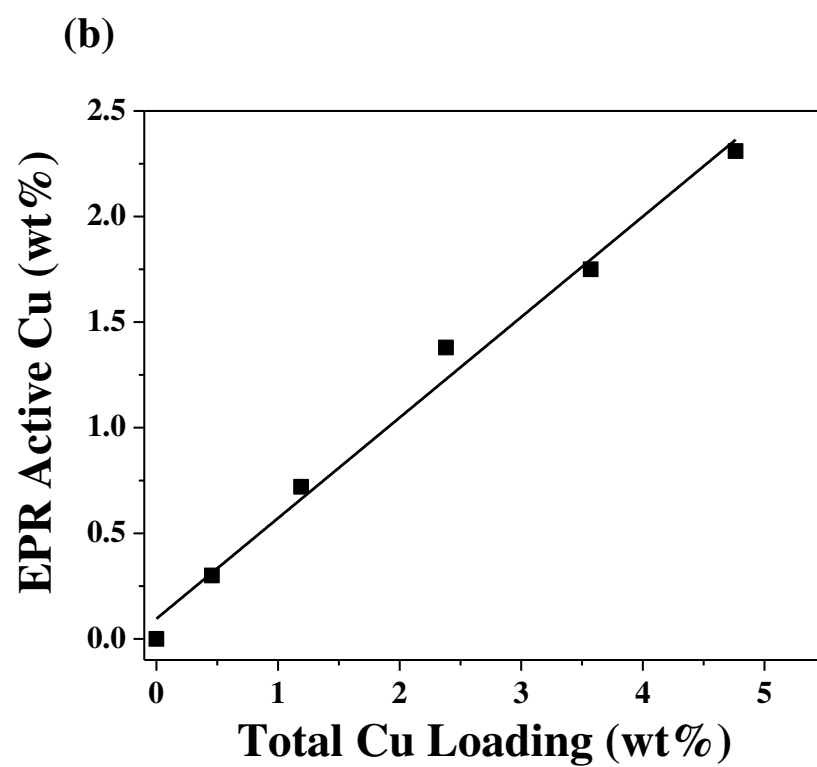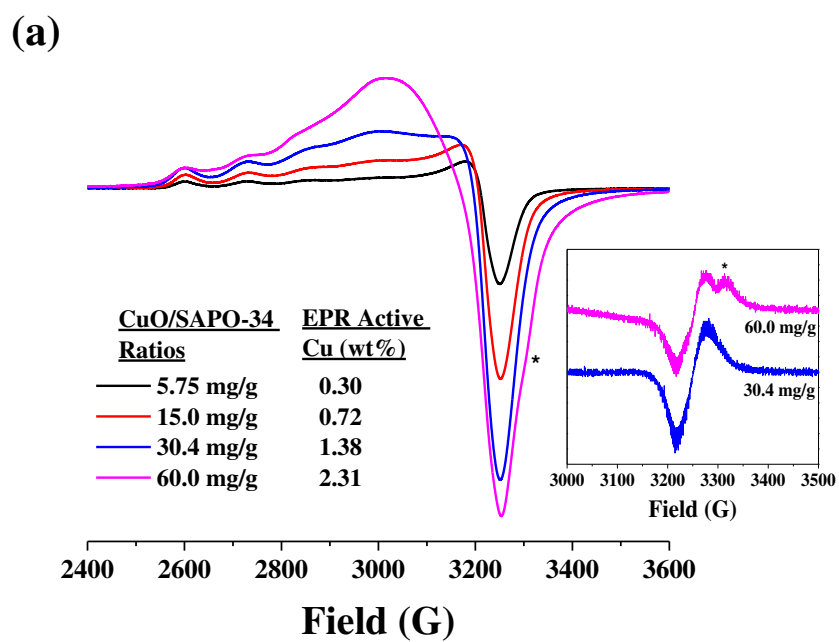
Figure 4, Gao, Walter, Washton, Szanyi, Peden

(a)

43   16   -9   -57

SAPO-34-ACS

5.75 mg CuO/g

15.0 mg CuO/g

30.4 mg CuO/g

60.0 mg CuO/g

120 100 80 60 40 20 0 -20 -40 -60 -80

^{27}Al Frequency (ppm from AlCl$_3$ (aq))

(b)

- 28

^{31}P-H$_2$O

SAPO-34-ACS

5.75 mg CuO/g

15.0 mg CuO/g

30.4 mg CuO/g

60.0 mg CuO/g

0   -20   -40   -60

^{31}P Frequency (ppm from H$_3$PO$_4$)

(c)

-89   -110

SAPO-34-ACS

5.75 mg CuO/g

15.0 mg CuO/g

30.4 mg CuO/g

60.0 mg CuO/g

0   50   -100   -150   -200

^{29}Si Frequency (ppm from TMS)
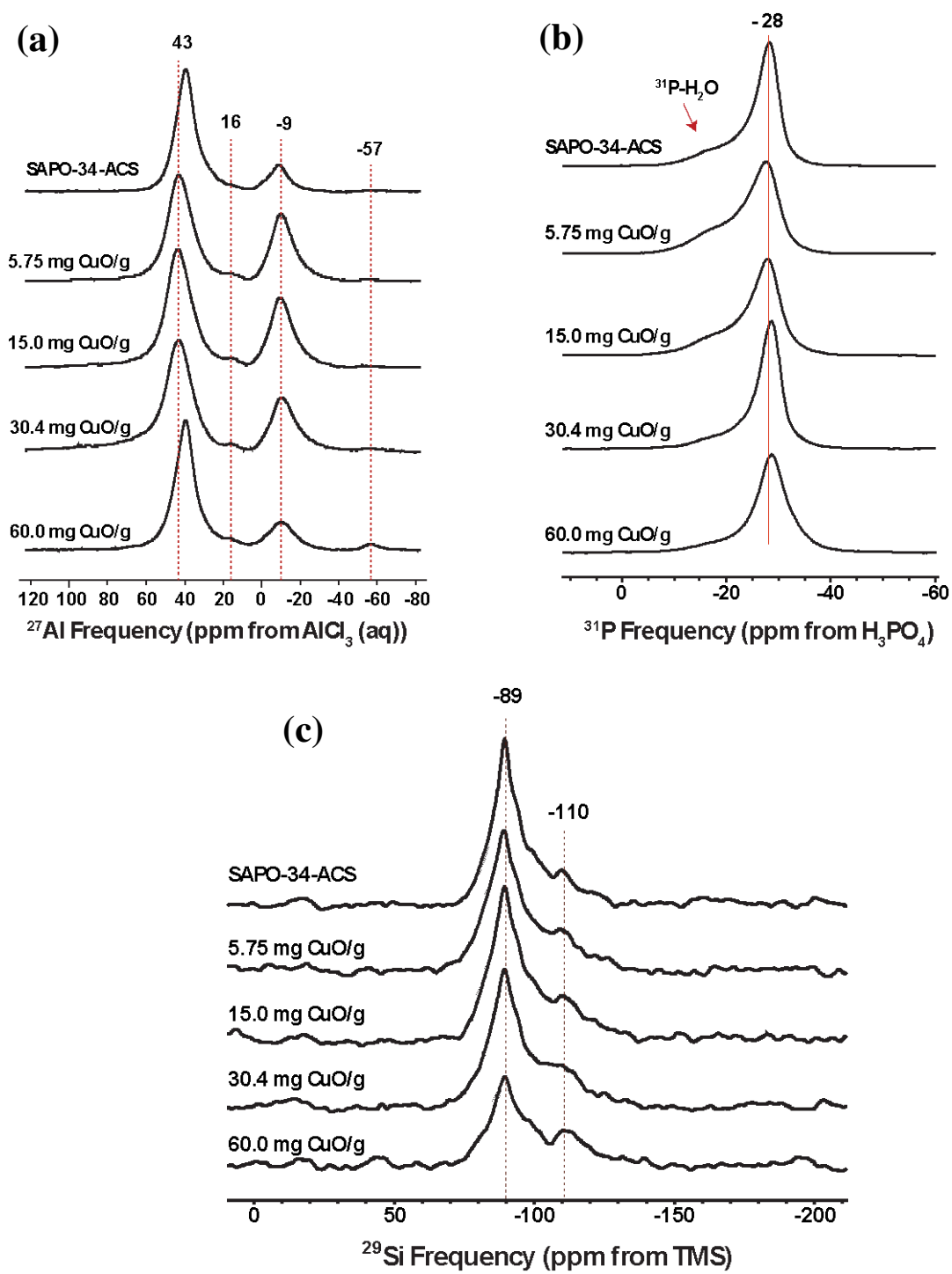
Figure 5, Gao, Walter, Washton, Szanyi, Peden

41

(a)

(b)
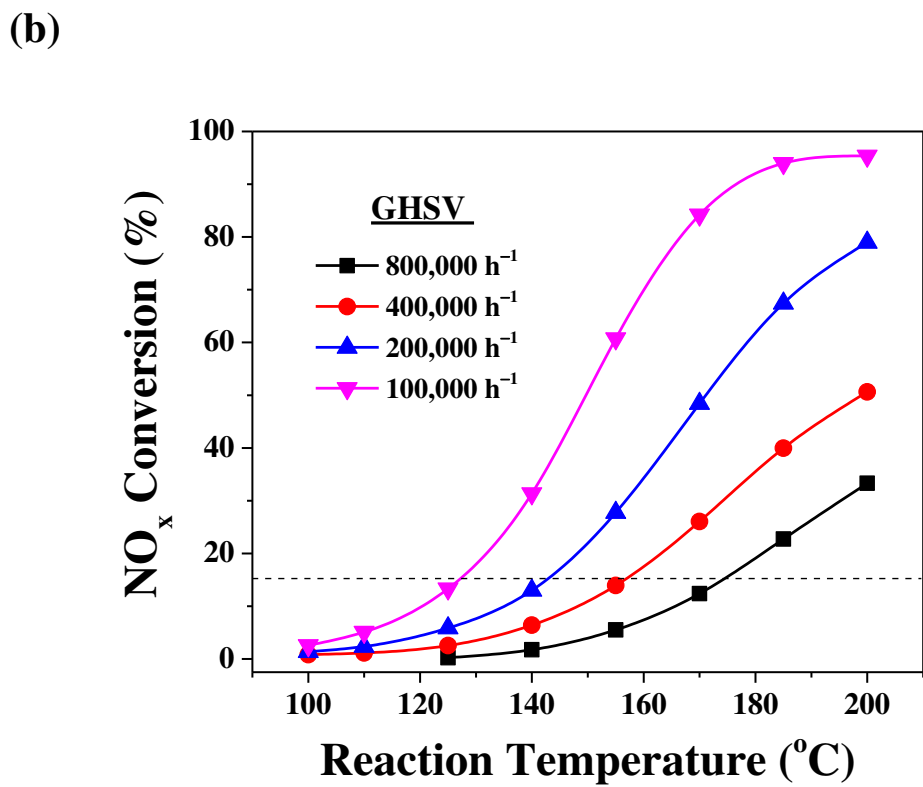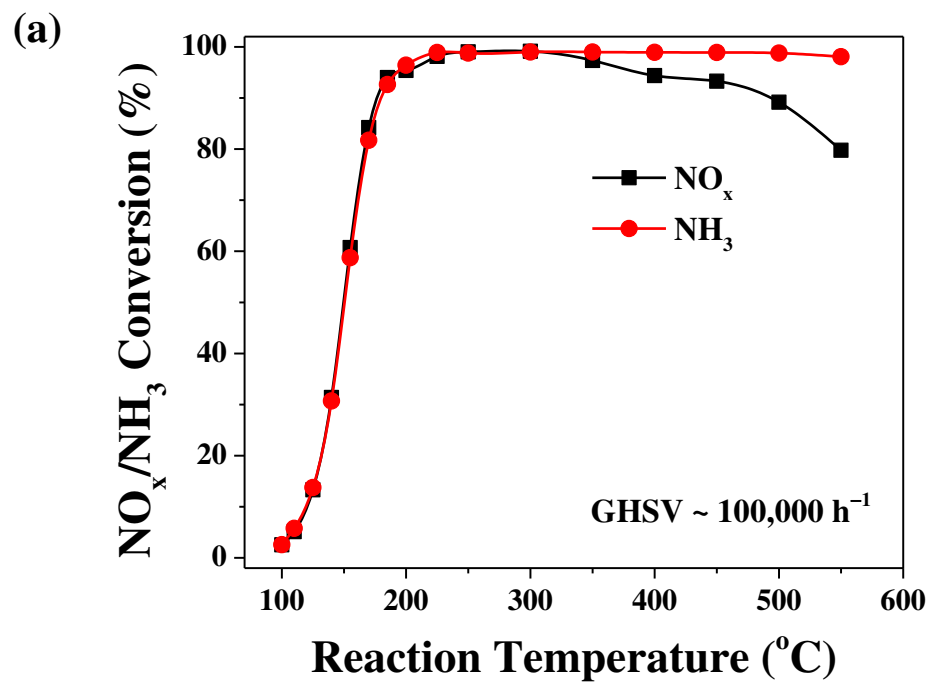
Figure 6, Gao, Walter, Washton, Szanyi, Peden

(a)

(b)
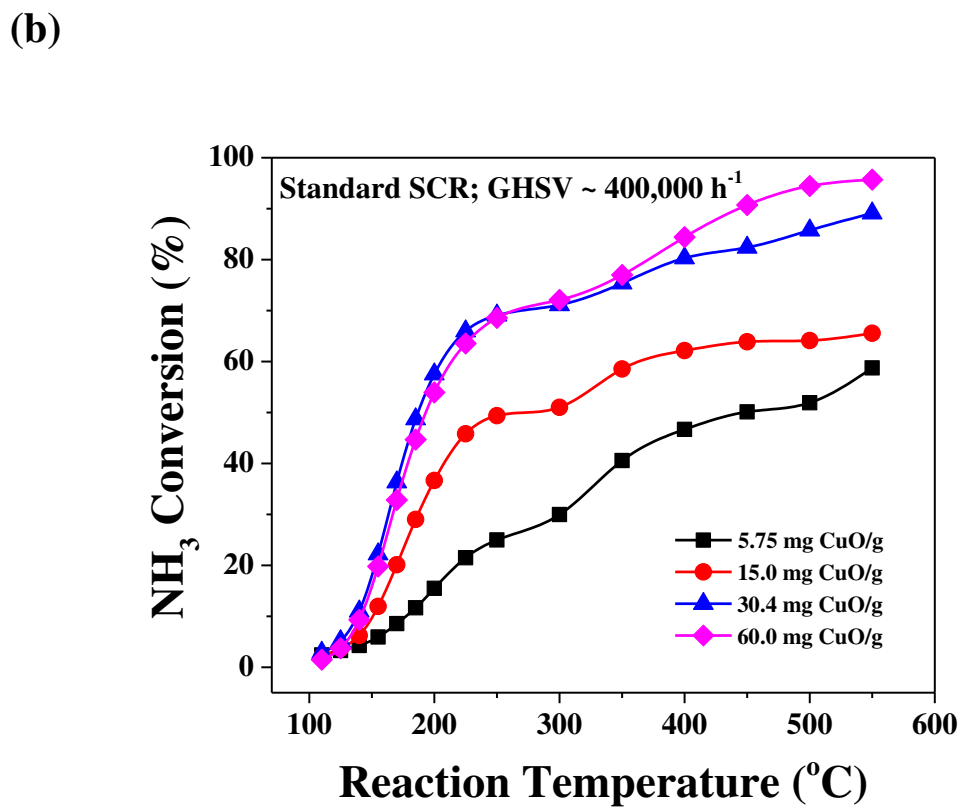
Figure 7, Gao, Walter, Washton, Szanyi, Peden
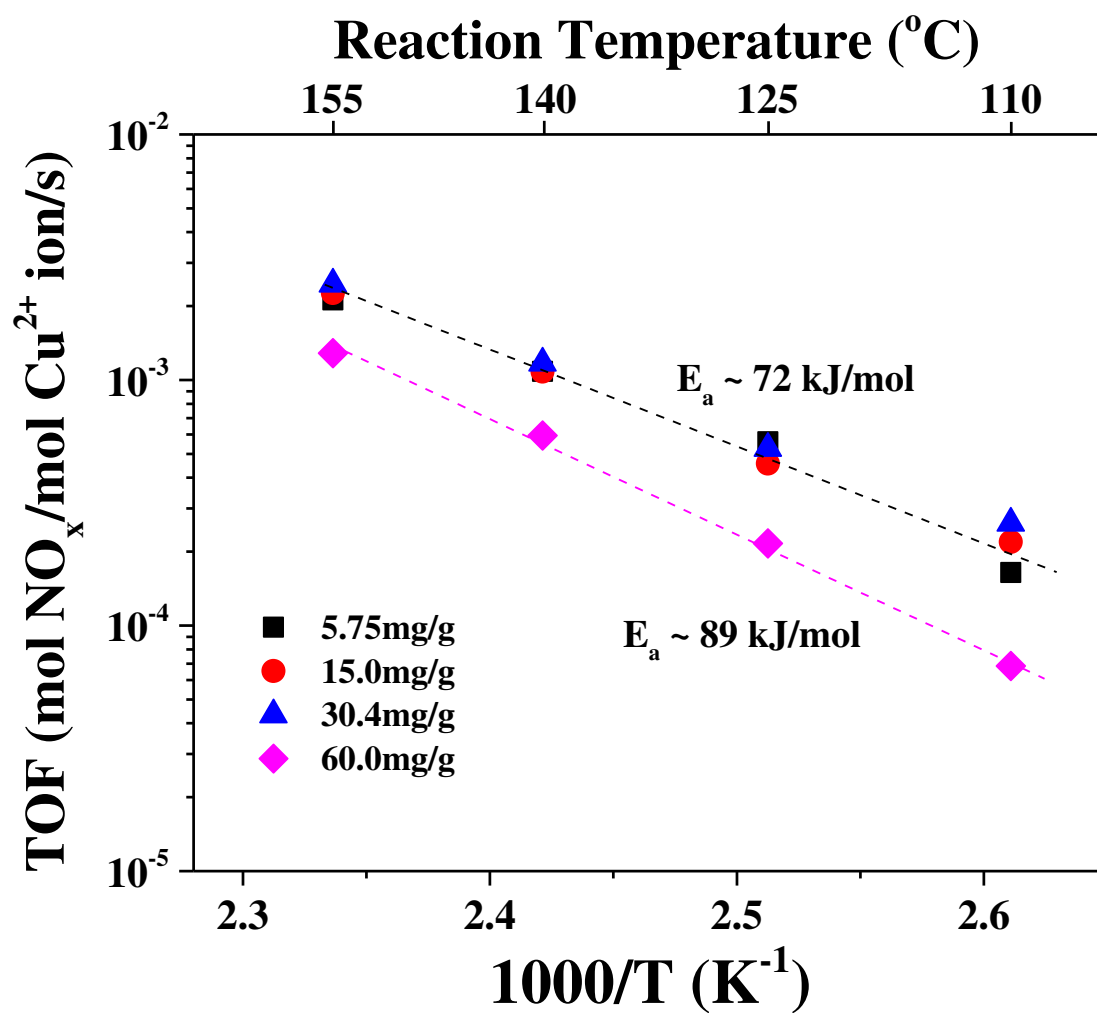
Figure 8, Gao, Walter, Washton, Szanyi, Peden

(a)
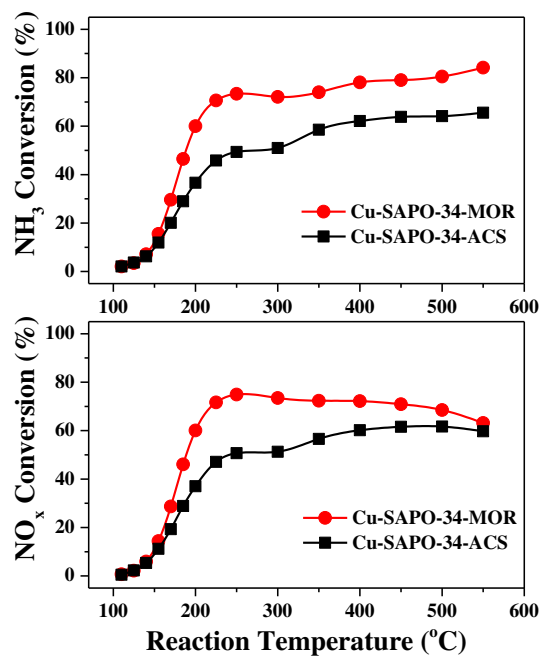
(b)
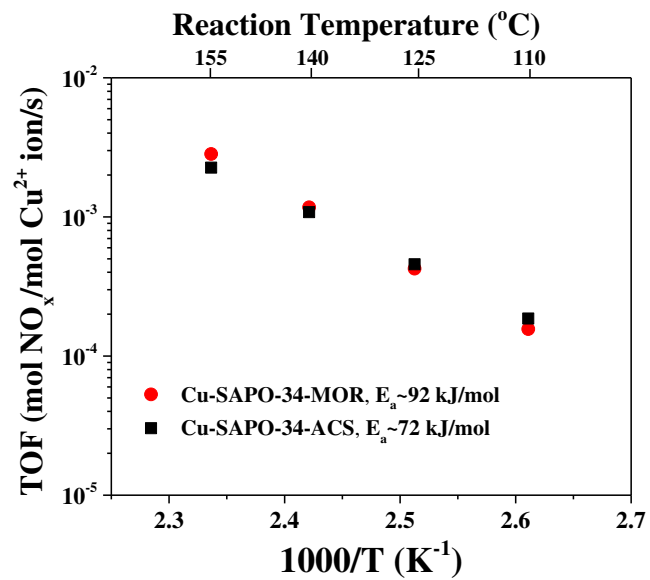
Figure 9, Gao, Walter, Washton, Szanyi, Peden

(a)
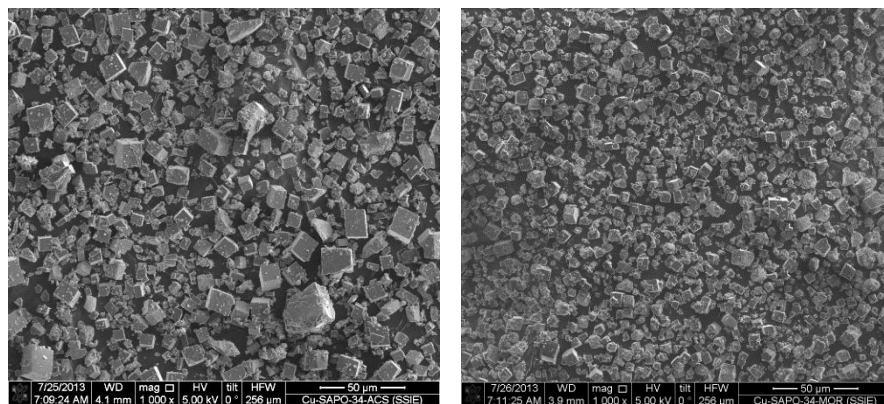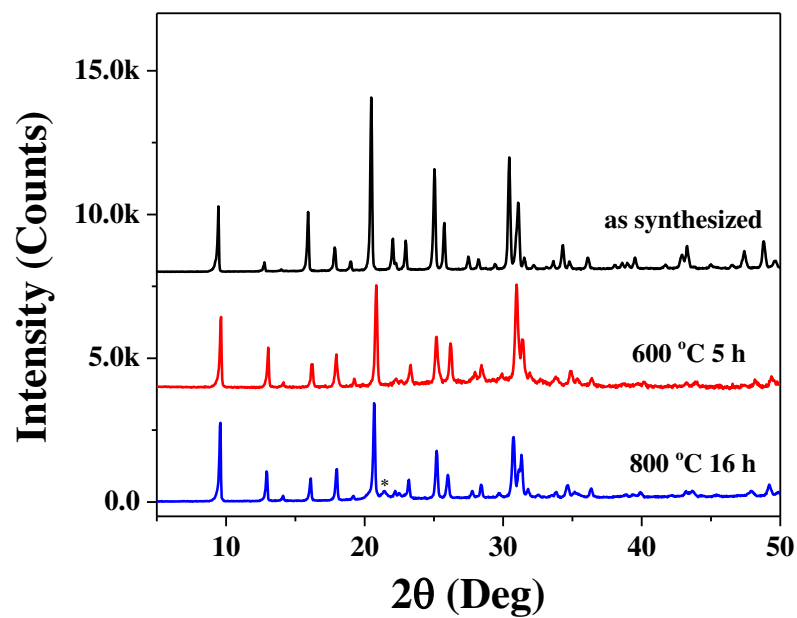

Cu-SAPO-34-ACS   Cu-SAPO-34-MOR

(b)
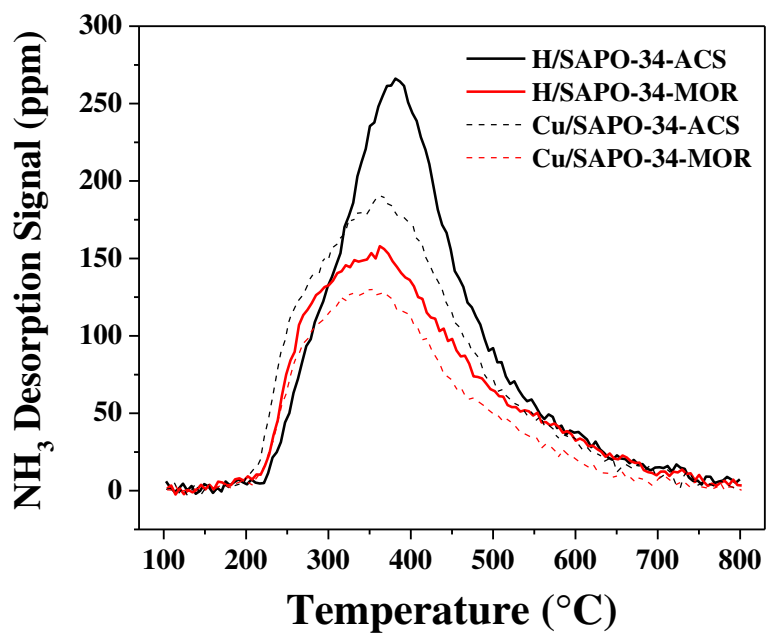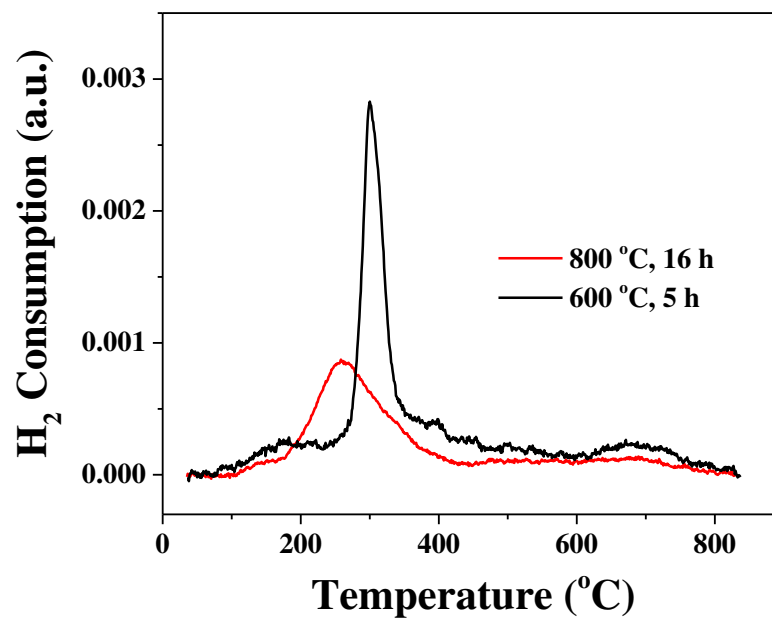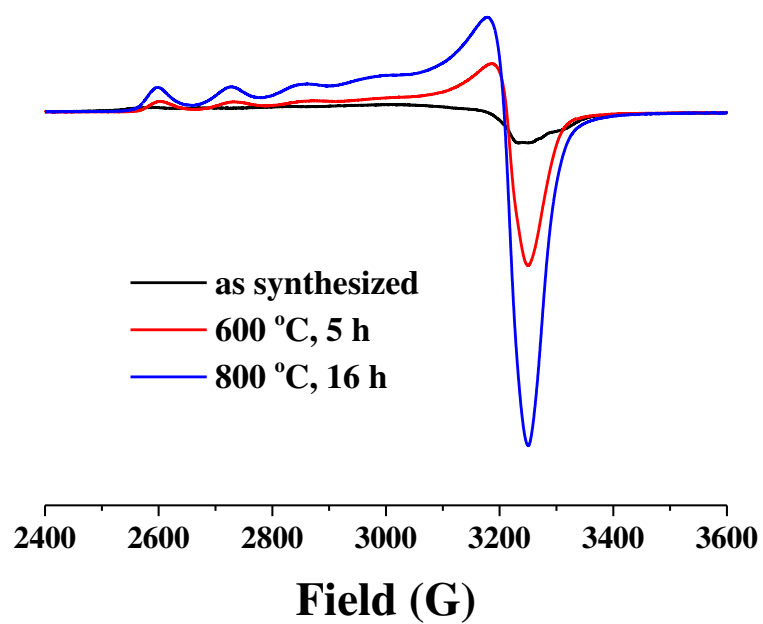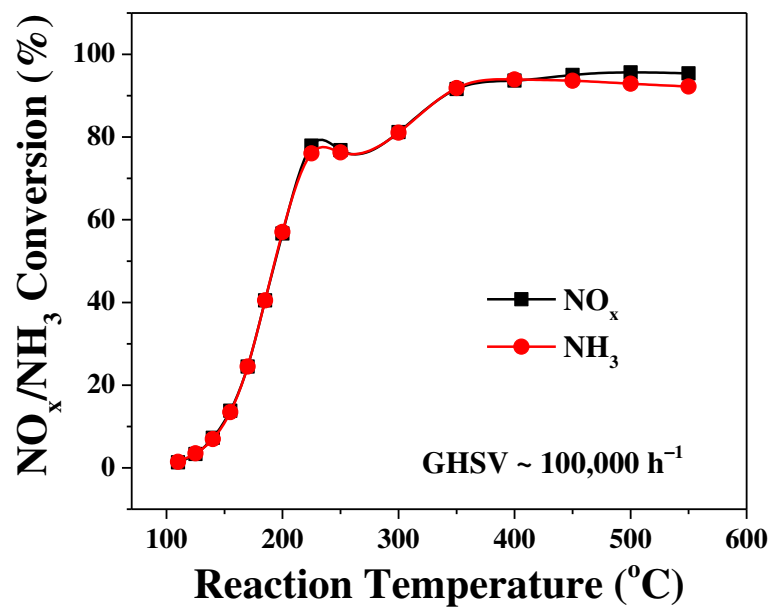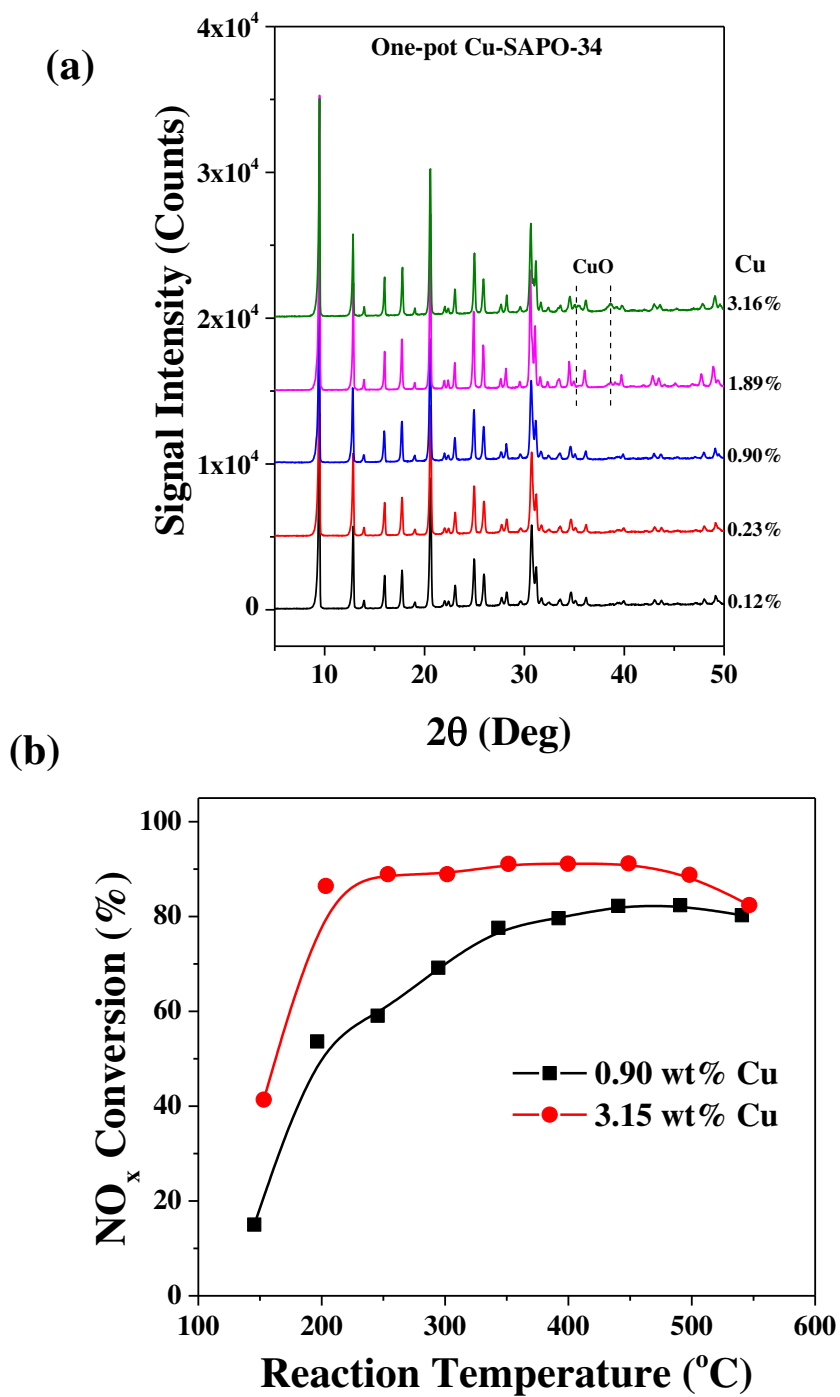

Figure 10, Gao, Walter, Washton, Szanyi, Peden

(a)

(b)

Figure 11, Gao, Walter, Washton, Szanyi, Peden

(a)

(b)

Figure 12, Gao, Walter, Washton, Szanyi, Peden

(a)

One-pot Cu-SAPO-34

CuO   Cu

3.16%

1.89%

0.90%

0.23%

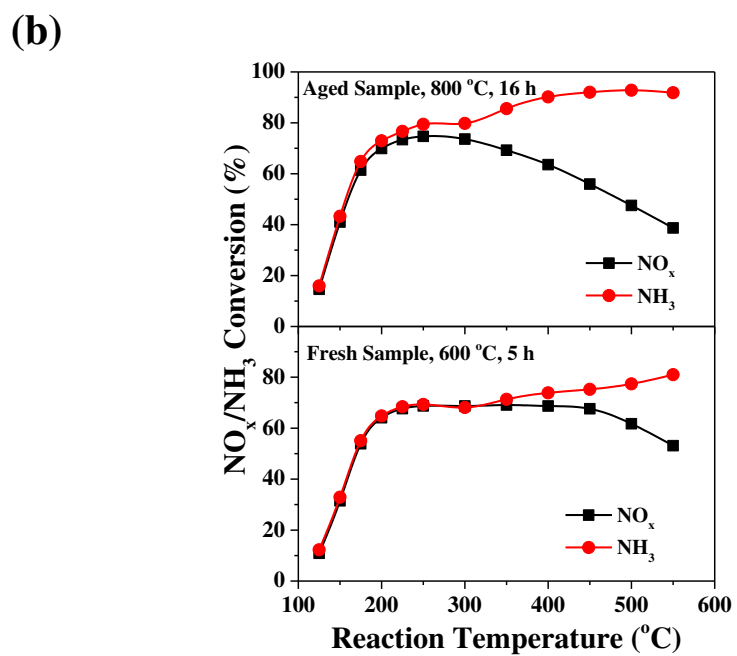0.12%

(b)
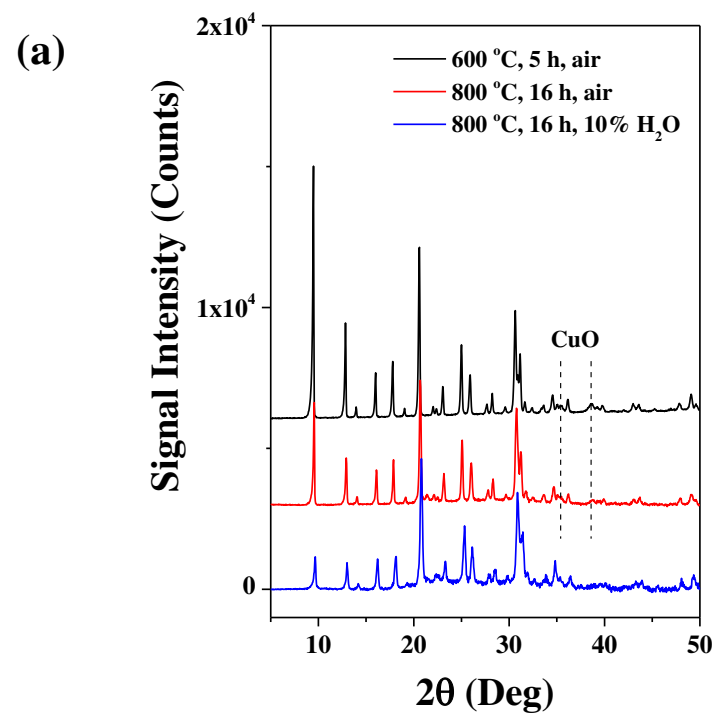
Figure 13, Gao, Walter, Washton, Szanyi, Peden

(a)

(b)

Figure 14, Gao, Walter, Washton, Szanyi, Peden

TOC

$$\text{H-SAPO-34} + \text{CuO} \rightarrow \text{Cu-SAPO-34} + \text{H}_2\text{O}$$